



Autonomic Biomolecular Materials for Sensing, Actuation, and Energy

Donald Leo
VIRGINIA POLYTECHNIC INST AND STATE UNIVERSITY

04/11/2020
Final Report

DISTRIBUTION A: Distribution approved for public release.

Air Force Research Laboratory
AF Office Of Scientific Research (AFOSR)/ RTB2
Arlington, Virginia 22203
Air Force Materiel Command

DISTRIBUTION A: Distribution approved for public release.

REPORT DOCUMENTATION PAGE			<i>Form Approved</i> <i>OMB No. 0704-0188</i>		
<p>The public reporting burden for this collection of information is estimated to average 1 hour per response, including the time for reviewing instructions, searching existing data sources, gathering and maintaining the data needed, and completing and reviewing the collection of information. Send comments regarding this burden estimate or any other aspect of this collection of information, including suggestions for reducing the burden, to Department of Defense, Executive Services, Directorate (0704-0188). Respondents should be aware that notwithstanding any other provision of law, no person shall be subject to any penalty for failing to comply with a collection of information if it does not display a currently valid OMB control number.</p> <p>PLEASE DO NOT RETURN YOUR FORM TO THE ABOVE ORGANIZATION.</p>					
1. REPORT DATE (DD-MM-YYYY) 08-06-2020		2. REPORT TYPE Final Performance		3. DATES COVERED (From - To) 15 Sep 2012 to 31 Oct 2018	
4. TITLE AND SUBTITLE Autonomic Biomolecular Materials for Sensing, Actuation, and Energy			5a. CONTRACT NUMBER		
			5b. GRANT NUMBER FA9550-12-1-0464		
			5c. PROGRAM ELEMENT NUMBER 61102F		
6. AUTHOR(S) Donald Leo			5d. PROJECT NUMBER		
			5e. TASK NUMBER		
			5f. WORK UNIT NUMBER		
7. PERFORMING ORGANIZATION NAME(S) AND ADDRESS(ES) VIRGINIA POLYTECHNIC INST AND STATE UNIVERSITY 300 TURNER ST NW, SUITE 4200 BLACKSBURG, VA 24061-0001 US			8. PERFORMING ORGANIZATION REPORT NUMBER		
9. SPONSORING/MONITORING AGENCY NAME(S) AND ADDRESS(ES) AF Office of Scientific Research 875 N. Randolph St. Room 3112 Arlington, VA 22203			10. SPONSOR/MONITOR'S ACRONYM(S) AFRL/AFOSR RTB2		
			11. SPONSOR/MONITOR'S REPORT NUMBER(S) AFRL-AFOSR-VA-TR-2020-0003		
12. DISTRIBUTION/AVAILABILITY STATEMENT A DISTRIBUTION UNLIMITED: PB Public Release					
13. SUPPLEMENTARY NOTES					
14. ABSTRACT <p>New stimuli-responsive materials and material systems were developed along with the fundamental understanding of transduction behavior. Stimuli-responsive behavior was introduced by the incorporation of biomolecules into polymeric materials, creating new means of measuring mechanical, electrical, chemical, and optical behavior. Nanoscale behavior of confined fluids and ion channels was modeled using molecular dynamics and coarse-grained simulations. Nanoscale simulations were utilized to understand how modifications of ion channels could be utilized to tailor the response to various stimuli. The first demonstration of mechanosensitive behavior in an artificial membrane was obtained, leading to new understanding of the dielectric behavior of mechanosensitive channels. Multiple fabrication techniques were developed that enabled the incorporation of biomolecules into solid substrates, microfluidic systems, and on oil-infused surfaces to create a wide arrange of materials and material systems. Macroscale models were developed to enable the design of biomolecular networks and linear and nonlinear analysis techniques were applied to the analysis of stimuli-responsive behavior. Comparisons between experimental results and macroscale simulations demonstrated the viability... Of en_ginring design for biomollw systems.</p>					
15. SUBJECT TERMS Biomolecular Materials, Stimuli-responsive Properties, Sensing and Actuation, Energy Transduction					
16. SECURITY CLASSIFICATION OF:		17. LIMITATION OF ABSTRACT	18. NUMBER OF	Standard Form 298 (Rev. 8/98) Prescribed by ANSI Std. Z39.18	

DISTRIBUTION A: Distribution approved for public release.

a. REPORT Unclassified	b. ABSTRACT Unclassified	c. THIS PAGE Unclassified	UU	PAGES	19a. NAME OF RESPONSIBLE PERSON LEE, BYUNG <hr/> 19b. TELEPHONE NUMBER <i>(Include area code)</i> 703-696-8483
----------------------------------	------------------------------------	-------------------------------------	----	--------------	---

Basic Research Initiative: Autonomic Biomolecular Materials for Sensing, Actuation, and Energy Conversion

Award Number: FA9550-12-1-0464

Organization: Virginia Tech

Principal Investigator: Donald J. Leo

Final Report

Project Overview

This program developed a new class of multifunctional materials for autonomic structures based on the stimuli-responsive properties of biomolecules. Our research enabled greater fundamental understanding of the transduction properties of certain transmembrane peptides and proteins under a variety of stimuli such as applied electrical fields, chemical gradients, mechanical force, and optical stimulus for the purpose of incorporation into multiscale response models. Novel fabrication processes led to a new class of flexible, monolithic structural material that incorporate tailored biomolecular networks for controlled ion and mass transport. Multiscale models of biomolecular networks were combined with a new understanding of biomolecular transduction for the purpose of creating novel materials with multifunctional sensing, actuation, and energy conversion properties.

Motivation

The Air Force has invested heavily over the past twenty years in research that utilizes stimuli-responsive materials to create multifunctional structures and systems. Notable applications include the development of sensor-infused platforms, precision pointing systems for space applications, systems that utilize advanced control for suppression of noise and vibration, and self-healing composites.

These investments have concentrated on the use of materials that exhibit controllable property changes induced by an applied stimulus. Much of the research has focused on the use of synthetic materials such as piezoelectric, shape memory, and magnetostrictive materials that exhibit a controllable dimensional change under the application of an applied potential, material heating, or magnetic field. These material types enable a diverse range of sensing and actuation properties that enable new types of multifunctional behavior in materials. In many instances an external or embedded electronic control system is required to induce multifunctional behavior in a system, e.g., lightweight systems that also exhibit precision pointing or vibration suppression. More recently the concept of *autonomic systems* has been introduced through the novel use of materials that automatically respond to changes in their environment. An autonomic system does not require the use of a control system to induce stimuli-responsive behavior; the stimuli-responsive behavior is an inherent property of the material system. An example of an autonomic system is one which can ‘heal’ itself or prevent the onset of damage through chemically-induced changes in material properties. Inspired by natural systems that can automatically heal themselves without the need for centralized control, these self-healing materials utilize novel combinations of stimuli-responsive materials that cause chemical changes in the material to prevent damage or recover damage caused by external mechanical loads.

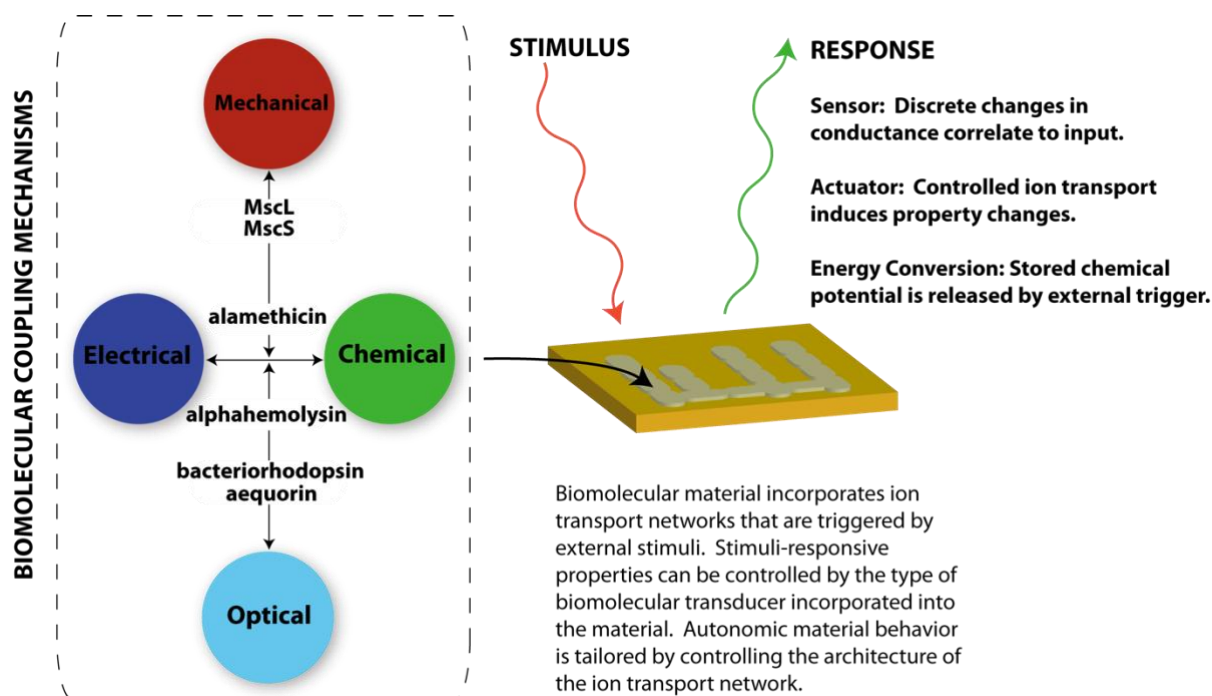


Figure 1: Biomolecular materials concept studied in this program.

Our program is also inspired by the way in which nature uses stimuli-responsive biomolecules to incorporate autonomic behavior in cellular systems. Cells are the basic building block of biological systems, and the autonomic behavior of many natural systems arises from the compartmentalization of cellular systems and the ability of cellular systems to communicate via charge and mass transport at cellular interfaces. In order to realize autonomic behavior, every cell tightly monitors internal and external parameters including cell volume, membrane area and tension, difference of water activities inside and outside, and volume fraction taken up by large macromolecular solutes. Understanding the principles and mechanisms that cells use to gauge and control bulk and interfacial parameters will allow us to exploit them for various applications. The pervasiveness of stimuli-responsive behavior in biomolecular processes leads us to the following question, “How can we utilize the stimuli-responsive biomolecules found in cells for the development of a new class of autonomic materials for sensing, actuation, and energy conversion?” It is our belief that this research will lead to a better fundamental understanding of how biomolecules can be assembled to make new types of materials, as well as the discovery of new knowledge on the ways that certain biomolecules respond to applied stimuli.

The vision for our program is to create a new class of materials and material systems that utilize the transduction properties of biomolecules to enable autonomic behavior. As shown in Figure 1, we envision creating a class of material that incorporates one or more internal networks of biomolecules whose transport properties can be controlled by external stimuli. Much like cellular systems, the network consists of numerous compartments and communication between compartments is controlled by the judicious choice of the biomolecule incorporated at the interfaces. It is well established through our work, and the work of others, that certain biomolecules such as transmembrane channels and pores exhibit transduction behavior between multiple physical domains. As shown in the left of Figure 1, incorporating these biomolecules

into the network allows us to couple the mechanical, electrical, chemical, and optical properties of the material. The introduction of stimuli-responsive materials will allow us to make new types of sensors where the frequency characteristics of the output are correlated to the input stimuli, or actuators that use controlled ion transport to induce property changes in the material, or novel energy conversion devices that can release stored chemical energy when triggered by an external mechanical or optical input. All of these behaviors are autonomic because they arise through the inherent properties of the biomolecules incorporated into the material.

Research Objectives

The research program had four primary research objectives:

- 1. Modeling and testing of stimuli-responsive biomolecules at the nanoscale to understand the insertion of transmembrane biomolecules into lipid bilayers and the response of the biomolecules to applied stimuli.**
- 2. Fabrication of networks of biomolecular unit cells at micrometer length scales and with increased functional density.**
- 3. Coupling of multiscale models to macroscale models that enable the design of biomolecular materials for sensing, actuation, and energy conversion.**
- 4. Characterization of biomolecular materials under a range of standardized conditions that enable direct comparison to the effectiveness of more traditional types of multifunctional materials.**

Significant Research Accomplishments

1. Fabrication of networks of biomolecular unit cells at micrometer length scales and with increased functional density.

The BRI program resulted in the development of multiple methods to fabricate materials and material systems that incorporated biomolecular transduction mechanisms. Automated 3D printing approaches were developed to enable the construction of bilayer networks. These techniques were combined with polymeric encapsulation technology to create solid-supported material systems that exhibited biomolecular transduction. Finally, microfluidic techniques were created to enable the organization of multi-bilayer networks with stimuli responsive properties.

Modified 3-D Printing Techniques

An off-the-shelf 3D printer was modified to support droplet-on-demand printing. A *LulzBot Taz 5* was purchased due to its open-source nature and low cost. A team of students then examined how to best modify the existing printing algorithm to accommodate droplet-on-demand printing rather than continuous extrusion.

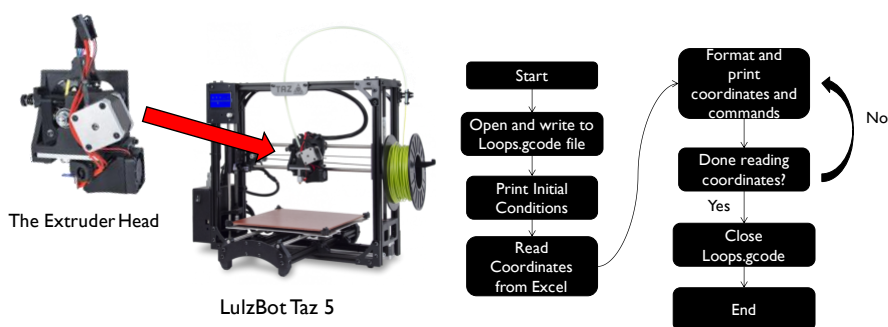


Figure 2 – Modified 3D printer for the creation of droplet networks and the accompanying algorithm.

The printer head was removed and replaced with a custom chamber allowing for dispensation of aqueous solution and an attached piezoelectric diaphragm for expelling droplets through pulses in the fluid. This was then connected to the original circuitry in the extruder head to use a

variable voltage supplied by the cooling fan controlled within the printer gcode. The gcode was then modified to produce deflections in the piezoelectric at desired points for droplet ejection through voltage impulses supplied to the piezoelectric.

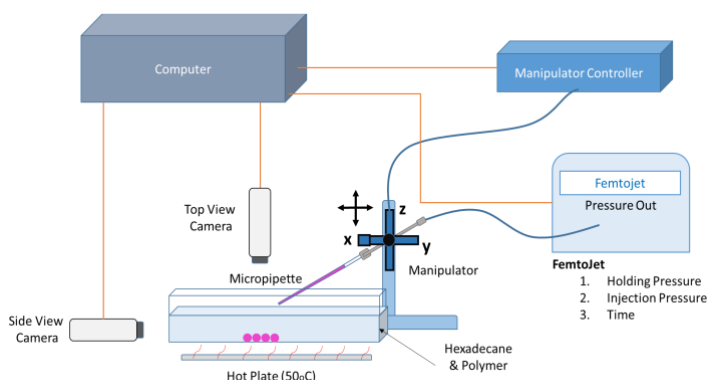


Figure 3 – Computer-controlled 3D printing using a pressure supply and motorized manipulator.

The team encountered difficulty producing the droplets due to insufficient voltage supplied to the piezoelectric diaphragm without substantial modifications. This is

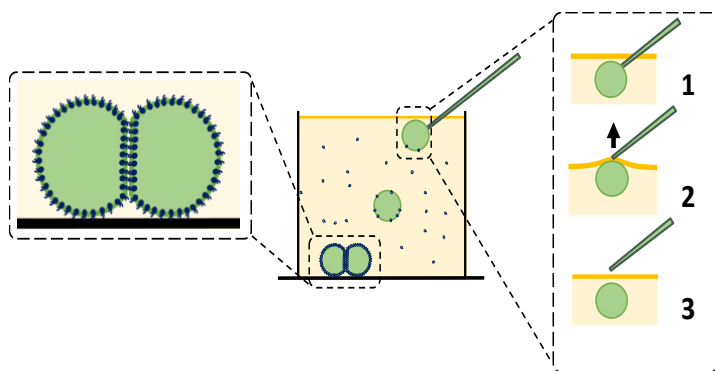


Figure 4 – Droplets are separated by capillary forces and settle within the oil after accumulating lipids on their surface.

currently being modified through another custom circuit to amplify the available voltage, as well as redesigning the printing needle to better translate the piezoelectric displacement to the fluid to improve droplet ejection (5).

Organogel Encapsulation

Due to the challenges faced by the modified 3D printer, an alternative approach was suggested using an available 3-axes motorized

manipulator and pressure supply. Both of these instruments communicate via serial port communications and may be controlled in parallel. Initially a script was created in BASIC to automate positioning of the head and subsequent droplet ejection from the pressure supply. This was then rewritten in MATLAB for ease of use, and for simultaneous communication with a National Instruments MyDAQ for voltage outputs as well to control additional instruments. The end result is a computer-controlled system for droplet printing with high precision with droplet dimensions as small as 100 microns in diameter.

While this printer is unable to eject droplets directly due to the limited time resolution offered by the pressure supply, an algorithm was produced that uses capillary force at the oil-air interface to remove the droplets from the tip of the printing needle, moving the tip up and out of the oil to separate droplets from the pipette. The droplets then fall into place, accumulating a coating of lipids as they descend through the oil. A custom pipette pulling algorithm was developed to ensure 30 micron diameter printing tips at all times, ensuring uniformity in droplet sizes with the applied pressures.

Printing patterns are specified in either Excel or text files by the user, and the printer generates matching droplet patterns automatically. This allows for testing the behavior of large droplet networks, and moving towards 3D structures. Conductive pathways containing alpha hemolysin were printed in multi-droplet networks, and tests of signal transduction along these pathways were examined. This method increased the size of the available networks by an order of magnitude, and allowed for much smaller droplets than previous approaches approaching appropriate scales for the development of synthetic tissues. Future work will involve improving the speed of the printing process by separating the droplets from the printing needle within the oil.

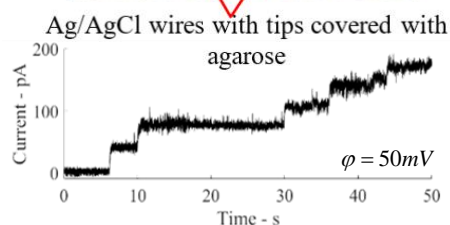
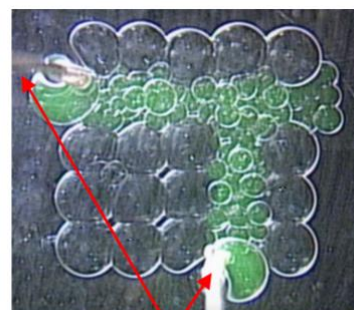


Figure 5 – Large droplet networks with embedded conductive pathways created with the printer.

Ongoing work includes optimizing printing within a styrene/(ethylene-butylene) based block copolymers (SEBS) and hexadecane mixtures to allow for encapsulated DIB networks and



Figure 6 – A self-supporting cube of organogel containing lipid-coated droplets.

structures (4). Dissolving this triblock copolymer within the oil phase creates a thermoplastic organogel that solidifies at room temperature without disturbing the droplets and their connective membranes. The goal is the production of self-supporting materials containing the synthetic tissues of stimuli-responsive membranes described in the previous task.

Combining this with the printing algorithm requires several modifications. For a self-supporting gel at room temperature, the concentration of the SEBS within the oil is considerable, raising the necessary melt temperature considerably. However temperatures above 60 °C risk damaging the channels and lipids. Consequently printing must be done at a lower temperature, resulting in a highly viscous solution. Secondly, the traditional 50/50 oil solution containing hexadecane and silicone oil AR20 is not available since SEBS and silicone oil are incompatible. As a result, only hexadecane is used. This greatly amplifies gravitational forces in addition to reducing the adhesive strength in the membranes, and requires additional care in printing the droplets.

Ongoing work includes characterizing the rheological properties of the organogel to identify the optimum concentration of SEBS within the oil that transitions at temperatures lower than 60 °C, while remaining self-supporting. This is accompanied by testing mixtures of spatially varying SEBS concentrations that later diffuse and solidify after printing is finished.

Microfluidic Organization of Networks

Our third approach to advance the design, assembly and use of unit-cell based autonomic materials applies principles of fluid flow in microfluidic channels to rapidly create, route, and connect pairs of lipid-coated droplets to form arrays of DIBs. In the past three years, we have designed and fabricated microfluidic devices (Figure 7A) that do just this, where pumping oil and aqueous solutions into channels within the devices generates streams of droplets, hydrodynamic traps designed using an electrical circuit model capture pairs of droplets from this stream to allow DIB formation, and thin-film electrodes deposited onto the underlying glass substrate enable independent electrical stimulation and interrogation of many DIBs in parallel. These findings were published in a 2016 Lab on Chip paper, where we demonstrated the rapid assembly and simultaneous interrogation of 8 symmetric DIBs (i.e. both droplets in a pair had identical compositions).

A key advantage of this device’s design is its scalability; increasing the number of hydrodynamic traps does not affect droplet trapping efficiency or lead to unwanted pressure drops in the device that can eject droplets from their traps. Therefore, the scalable design enables a microfluidic device to permit the rapid assembly of very large networks of DIBs. However, its potential use in sensing or energy conversion applications was limited by the fact that every droplet in the array had an identical composition. Instead, what is often desired to create a functional unit cell is to impose some asymmetry in a droplet pair, such that transmembrane proteins can insert into the bilayer in a specific direction, there exists a necessary solute concentration difference, different biomolecules exist on each side of the membrane, or even that the two leaflets of the bilayer contain different constituents. It is asymmetries such as these that allow for directional transport of ions for energy storage applications (e.g. proton currents driven by light-activated proteins). Therefore, our focus during the past year has been to enable the formation of asymmetric DIBs within a microfluidic environment by adding features that permit the formation of alternating droplet streams, sourced from more than one aqueous solution inlet.

Figure 7B shows the opposing T-junction design we selected and recently integrated into our microfluidic device. This approach enables the formation of a stream of alternating aqueous droplet compositions in an oil-filled channel when the device is operated within specific ranges of capillary number and volumetric water fraction. The horizontal inlet channel in Figure 3B contains oil while the two perpendicular, tapered channels are separate aqueous inlets. Both the oil and aqueous phases are injected at defined flow rates using syringe pumps, and the stream of produced droplets flow from left to right. Figure 3C shows an image of hydrodynamic traps (located downstream of the T-junctions) containing alternating, lipid coated droplets. A water-soluble food coloring added to one of the aqueous streams helps to distinguish droplet compositions. This provided an initial proof-of-concept that asymmetric droplets could be achieved in all pairs of an array. In addition, we performed measurements in a device that included electrodes (Figure 3D) in which one of the two droplets of each pair included

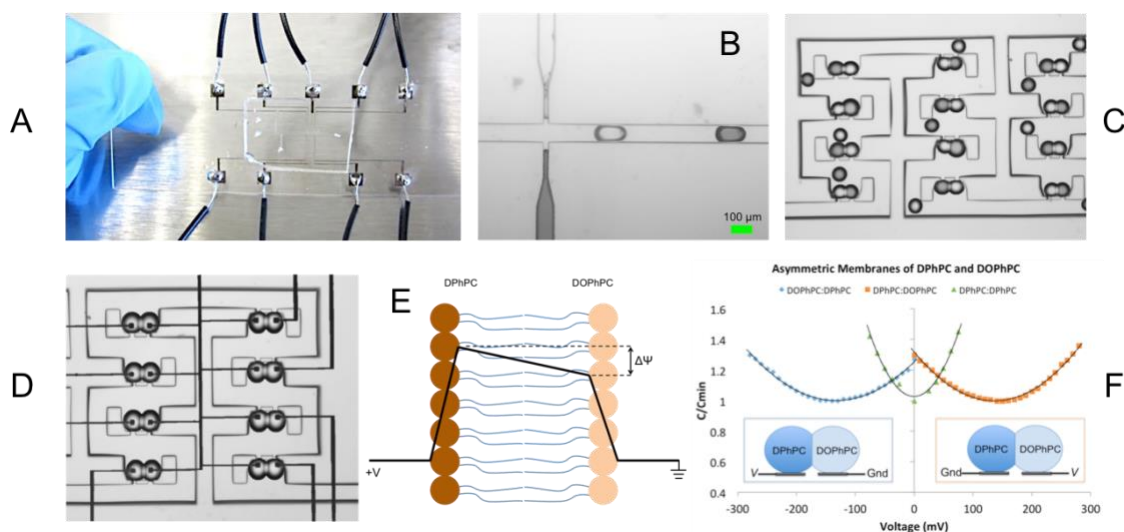


Figure 7: (A) Microfluidic device for DIB array formation and electrical interrogation. (B) Opposing T-junction inlet design for creating alternating droplet streams. (C) Asymmetric DIBs formed from alternating droplets in 12 sequential hydrodynamic traps. (D) Image of alternating DPhPC:DOPhPC droplets in electroded traps. (E) Electrical potential profile across a DPhPC:DOPhPC bilayer when zero volts are applied. (F) Measurements of membrane capacitance versus bias voltage for symmetric and asymmetric DIBs.

alamethicin, a voltage-dependent peptide that forms ion channels only at positive polarities. While not shown here, these measurements confirmed that utilizing alternating droplets compositions allow us to control the direction of both peptide insertion and ion transport in each DIB of an array.

However, to demonstrate that asymmetric membranes (i.e. those with different phospholipid compositions) could be achieved and to study lipid asymmetry in model membranes, we performed a third set of measurements in which each aqueous solution contained liposomes made from different phospholipids. We intentionally selected DPhPC and DOPhPC phospholipids as our two types, since these lipids are known to have different dipole potentials (350mV and 200mV, respectively). This potential difference, in addition to any applied voltage and any surface potential difference (none in this case for identical PC head groups on both leaflets), determines the total intramembrane potential as sketched in Figure 3E. Therefore, if the membranes are asymmetric, then we expected it to exhibit a $\sim|150\text{mV}|$ potential even when zero volts is applied between the electrodes. We utilized membrane electrowetting capacitance measurements versus varying dc bias voltages to detect this potential difference. Figure 3F shows the results of this measurement for both asymmetric DPhPC:DOPhPC and symmetric DPhPC bilayers. The voltage at which bilayer capacitance is minimum corresponds to the same magnitude but opposite sign as the intramembrane potential caused by the difference in dipole potentials. For example, with the DPhPC-containing droplet on the sensing (V) electrode, the minimum capacitance occurs at -137mV, which indicates that there is a +137mV bias with respect to the DOPhPC droplet resting on the ground electrode. This finding matches well to what has been measured previously. In contrast, symmetric membranes exhibit minimum capacitance at zero volts.

2. Modeling and testing of stimuli-responsive biomolecules at the nanoscale to understand the insertion of transmembrane biomolecules into lipid bilayers and the response of the biomolecules to applied stimuli.

Multiscale Methods for Structure

Aluru's group has pioneered the development of empirical potential-based quasi-continuum theory to predict the structure of confined fluids. Empirical potential-based quasi-continuum theory (EQT) provides a route to incorporate atomistic detail into continuum framework such as the Nernst-Planck equation. EQT can also be used to construct a grand potential functional for classical density functional theory (cDFT). The combination of EQT and cDFT provides a simple and fast approach to predict the inhomogeneous density, potential profiles, and thermodynamic properties of confined fluids.

During this program, we extended the EQT multiscale framework to model electrolytes under confinement. Since water is a highly polar solvent, electrostatic interactions of interfacial water molecules play a dominant role in determining the distribution of ions in electric double layers (EDLs). Near a surface, an inhomogeneous and anisotropic arrangement of water molecules gives rise to pronounced variations in the electrostatic and hydration energies of ions. Therefore, a detailed description of the structural and dielectric properties of water is important to study EDLs. However, most theoretical models ignore the molecular effects of water and treat water as a background continuum with a uniform dielectric permittivity. Explicit consideration of water polarization and hydration of ions is both theoretically and numerically challenging. In our work, we extended the empirical potential-based quasi-continuum theory for EDL, which incorporates the polarization and hydration effects of water explicitly. In EQT, water molecules are modeled as Langevin point dipoles and a point dipole based coarse-grained model for water was developed systematically. The space dependence of the dielectric permittivity of water is included in the Poisson equation to compute the electrostatic potential. In addition, to reproduce hydration of ions, ion-water coarse-grained potentials were developed. We demonstrated the EQT framework for EDL by simulating NaCl aqueous electrolyte confined inside slit-like capacitor channels at various ion concentrations and surface charge densities. We showed that

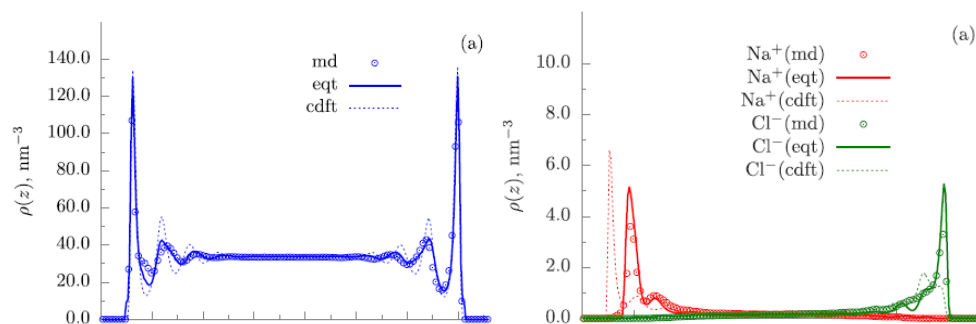


Figure 8: (left) Comparison of water density profiles obtained from molecular dynamics (MD) and EQT. The results from the widely used cDFT approach are also shown. (right) Comparison of sodium and chloride density profiles obtained from MD and EQT.

During this program we also extended the EQT framework to predict the thermodynamic properties of confined mixtures. The central idea in EQT is to construct potential energies that

integrate important atomistic details into a continuum-based model such as the Nernst-Planck equation. The EQT potentials are also used to construct the excess free energy functional, which is required for the grand potential in the classical density functional theory (cDFT). In our work, we use the EQT-based grand potential to predict various thermodynamic properties of a confined binary mixture of hydrogen and methane molecules inside graphene slit channels of different widths. We showed that the EQT-cDFT predictions for the structure, surface tension, solvation force, and local pressure tensor profiles are in good agreement with the molecular dynamics simulations. Moreover, we studied the effect of different bulk compositions and channel widths on the thermodynamic properties. Our results revealed that the composition of methane in the mixture can significantly affect the ordering of molecules and thermodynamic properties under confinement. In addition, we found that graphene is selective to methane molecules.

Multiscale Methods for Transport

During the latter part of the BRI program we formulated a one-dimensional isothermal hydrodynamic transport model for water. We incorporated the viscosity variations in confinement by using the local average density method. Dirichlet boundary conditions are provided in the form of slip velocity that depends upon the macroscopic interfacial friction coefficient. The value of this friction coefficient is computed using the generalized Langevin equation formulation that eliminates the use of equilibrium molecular dynamics simulation. We tested the approach on gravity driven flows of SPC/E water confined between graphene and silicon slit shaped nanochannels for low and high friction cases. The proposed model yields good quantitative agreement with the velocity profiles obtained from non-equilibrium molecular dynamics simulations (see Figure 9).

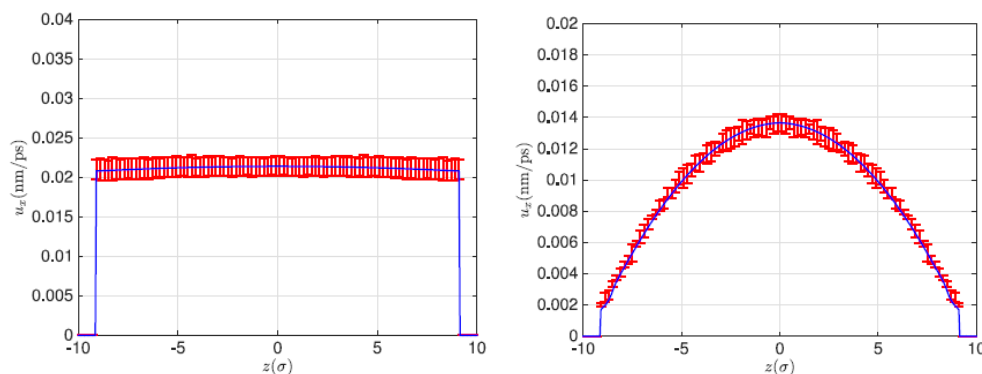


Figure 9: (left) Velocity profile of water in a graphene slit. (right) Velocity profile of water in a silicon slit. In both plots, molecular dynamics (MD) results are shown in error bars and solid line is the continuum result.

During the last year, we also developed an isothermal, one-dimensional, electroosmotic flow model for slit-shaped nanochannels. Nanoscale confinement effects are embedded into the transport model by incorporating the spatially varying solvent and ion concentration profiles that correspond to the electrochemical potential of mean force. The local viscosity is dependent on the solvent local density and is modeled using the local average density method. Excess contributions to the local viscosity are included using the Onsager-Fuoss expression that is dependent on the local ionic strength. A Dirichlet-type boundary condition was used in the form

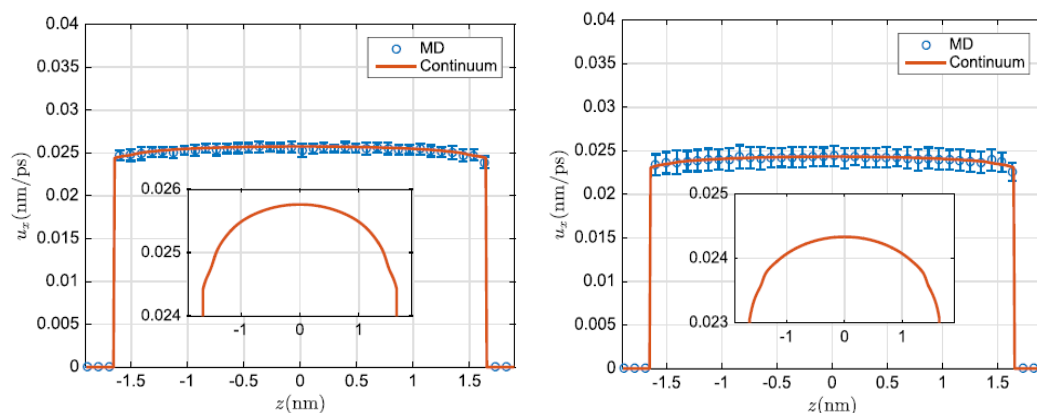


Figure 10: Electroosmotic flow velocity profiles for (a) sodium ions in a graphene channel and (b) chloride ions in a graphene channel. Multiscale theory results are in solid line (red), while MD results are represented by error bars (blue). Insets show the viscous contributions from the multiscale transport model to the EOF in more detail.

of the slip velocity that is dependent on the macroscopic interfacial friction. This solvent-surface specific interfacial friction was estimated using a dynamical generalized Langevin equation based framework. The electroosmotic flow of Na^+ and Cl^- as single counterions and NaCl salt solvated in Extended Simple Point Charge (SPC/E) water confined between graphene and silicon slit-shaped nanochannels are considered as examples. The proposed model yields a good quantitative agreement with the solvent velocity profiles obtained from the non-equilibrium molecular dynamics simulations (see Figure 10).

Force-Fields for Water/Nanomaterial Interaction

Hexagonal boron nitride is currently being used for a number of applications in nanotechnology. The study of hexagonal boron nitride (hBN) for nanobiotechnology applications at the atomic level requires accurate force field parameters to describe the water-hBN interaction. During the last year, we performed benchmark quality first principles quantum Monte Carlo calculations on the interaction energy between water and hBN, which are used to validate random phase approximation (RPA) calculations (see Figure 11). We then proceeded with RPA to derive force field parameters, which were used to simulate water contact angle on bulk hBN, attaining a value within the experimental uncertainties. We have demonstrated that end-to-end multiscale modeling, starting at detailed many-body

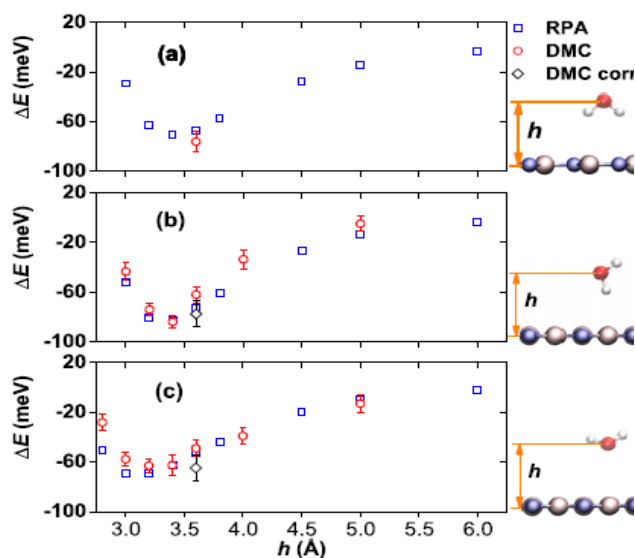


Figure 11: The interaction energies between hBN and water for three different water orientations. The results by diffusion Monte Carlo (DMC) are included for comparison. The DMC results at $h = 3.6 \text{ \AA}$ in (b) and (c) shifted by $16 \pm 8 \text{ meV}$ based on the finite size error correction for water orientation in (a) are labelled by “DMC corrected.”

quantum mechanics and ending with macroscopic properties, with the approximations controlled along the way, is feasible for these systems.

Modeling the dielectric properties of channels and associated membranes to understand the coupling mechanisms observed in the work by Najem and Leo.

Transmembrane voltage is a critical parameter for the function of many ion channels with two respects: (i) it provides the driving force for passing ions and (ii) it is a powerful factor in driving and modulating channel gating. Even channels that are not considered to be voltage-gated and lack canonical voltage sensors can be modulated by voltage acting on other domains. Here we describe a strong modulation of the bacterial mechanosensitive channel MscL, specifically its mild gain-of-function version (V23T), exerted through a dielectric mechanism by water present in the pore. Naturally, the channel functions as an osmolyte release valve in the inner bacterial membrane, which normally maintains high (100-160 mV) membrane potential. On the other hand, with its relatively simple structural design, MscL is considered a promising precursor for the development of ‘smart’ materials for sensory or energy conversion devices, and for this reason it must be well characterized in terms of its voltage dependence. The principles of electric field action on MscL conformational equilibrium should be equally well understood from the position of its in-vivo function as a ‘safety valve’, as well as from the point of view of bio-inspired material engineering.

The previously observed higher probability of opening events in the course of cyclic mechanical stimulation of the DIB-reconstituted MscL (V23T mutant) at membrane voltages above 80 mV (Najem et al.) motivated us to look more carefully at the voltage dependence of WT and V23T MscL. By performing patch-clamp measurements under linear pressure ramp stimulation at different voltages we were able to evaluate voltage contributions to the opening transition energy of these two channels. The data reveal that both versions of MscL have a dipole (linear with voltage) and a dielectric/capacitive (quadratic with voltage) contributions into the transition energy. The difference between WT and V23T is that WT exhibits a larger dipole and a considerably smaller dielectric contribution, whereas V23T shows a dominating dielectric contribution apparently related to a more pronounced pore hydration in the mutant. The changing hydration that influences the capacitive/dielectric energy imparts an energetic effect that depends on both the volume of polarized water and on the electric field distribution in the hydrated pore in the closed, expanded (subconductive), and open states. The voltage, and more specifically the portion of the electric field that drops inside the hydrated pore, drives opening by favoring high-dielectric water that displaces the lower-dielectric protein in the constriction. Flattening of the protein and nearby lipids also add a noticeable contribution as they increase the effective capacitance of that region and thus are favored – by voltage. The reorientation of protein-associated dipoles with channel opening and the changes in the external electric field around the protein and annular lipids both bring a measurable polarity-dependent contribution to the gating energy, either favoring or disfavoring opening, depending on the polarity of the external field and the particular conformation of the channel. To explore the nature of the electric field that influences the open probability further, we have compared V23T MscL behavior in electrically symmetric and asymmetric DIBs where a large (~140 mV) constant intrinsic bias was created by using lipids with different dipole potentials. The data obtained in DIBs confirm that V23T MscL senses local intramembrane electric fields in the membrane core outside of the interfacial (dipole) layers, but not directly the external voltage imposed by electrodes. Our results emphasize that massive changes in pore hydration, as in V23T MscL, can bring a considerable

dielectric contribution to the gating energy, which must be taken into account for the ‘native’ and ‘engineered’ valve functions. The electric field that is sensed by the channel is localized inside the (low-dielectric) core of the membrane,

Results

Figure 12 depicts activation curves of WT and V23T MscL populations recorded using standard patch-clamp technique in inside-out patches excised from giant spheroplasts (~30-50 channels/patch). The mechanical stimulus is a linear ramp of pressure from zero to saturating level (~250 mm Hg) recorded at different voltages. One can see that in wild-type MscL (panel a) the midpoint for population activation does not change much at negative pipette voltages (asterisk), but shifts to the left with positive voltage. In V23T MscL, in contrast, the midpoint shifts considerably to the left under both voltages. With the notion that tension midpoint at low voltages (near zero) for WT and V23T MscL resides at 12 and 8.3 mN/m, respectively, and assuming that the patch geometry (curvature) in all trials within each experiment remains the same, reduction of midpoint tension $\gamma_{0.5}$ can be interpreted as a reduction of the effective energy for the closed \rightarrow open transition. Also there is an interesting common feature: notably, both channels show ‘lingering’ conductive states at high negative voltages after stimulating pressure is released (black arrows).

From the Boltzmann-type relationship for the closed and open probabilities $P_o/P_c = \exp(-(E_o - \gamma\Delta A)/kT)$ one can see that at the midpoint ($\gamma_{0.5}$ tension) $P_o=P_c$ and therefore the transition energy in the absence of tension $E_o = \gamma_{0.5}\Delta A$. The fact that $\gamma_{0.5}$ decreases with voltage indicates that there must be a voltage-dependent term (or terms) in the transition energy. As seen from panel c, for WT the voltage dependent term is negative at positive voltages and slightly positive at negative voltages. For V23T, the V-dependent term is always negative at both voltages (more pronounced at positive potential) and the $E_o(V)$ dependence can be reasonably fitted with a parabola with a dominating negative quadratic term (panel d). The parabolic fit of the WT dependence indicates a larger linear term (panel c). The linear and quadratic terms can be physically interpreted as the dipolar (E_d) and dielectric (capacitive, E_c) contributions of electric polarization of the system and thus the transition energy in the absence of tension can be written as $E_o = E_i + E_d(V) + E_c(V^2)$, where E_i is the voltage-independent term estimated at low voltages. The general form the energy E_d of a dipole \vec{p} in a uniform electrostatic field \vec{E} is:

$$E_d = \vec{p} \times \vec{E}$$

However, the external electrostatic field around MscL channel is very non-uniform due to the different geometries and dielectric properties of the pore, the protein, and the annular lipids subjected to distortion. With that, a more convenient approximation would be to consider the dipole as a system of two-point charges at a distance d , each of them at a certain potential level of the external field (V_a and V_b):

$$E_d = \frac{p}{d} (V_a - V_b)$$

The dielectric effect is dominated by the displacement of a part of the protein by water. For a cylindrical capacitor of radius r and thickness h filled with a medium of dielectric permeability ϵ with an applied voltage, the energy E_c can be expressed as:

$$E_c = \frac{\epsilon\epsilon_0\pi r^2}{2h} V^2$$

For MscL in a membrane, the total dielectric contribution to energy will be composed of three parts - due to flattening of the protein barrel (E_b) along with annular lipids (E_a), and polarization of water that displaces the protein and fills the open pore interior (E_i) the equation can be written in the form:

$$E_c = E_a + E_b + E_i$$

More detailed calculations for the dipole and dielectric contributions into the system energy for different conformational states of WT and V23T MscL can be found in the supplement.

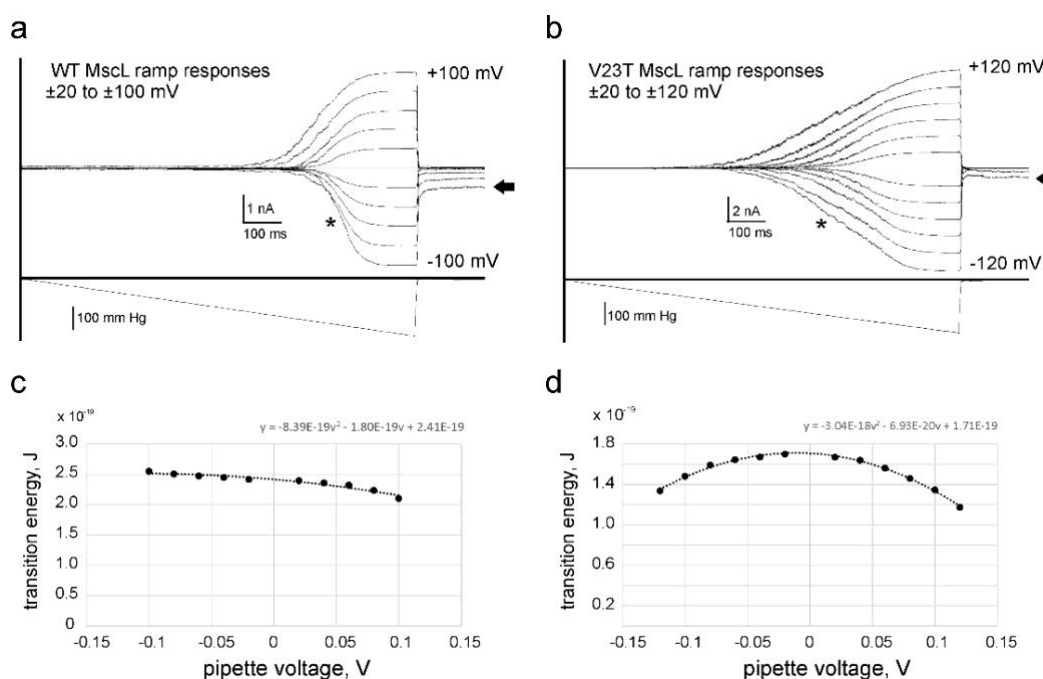


Figure 12. Voltage sensitivity of MscL. Current responses of WT MscL and V23T MscL populations to pressure ramps at different pipette voltages (imposed with 20 mV increments). Experiments were conducted in inside-out patches excised from giant bacterial spheroplasts expressing corresponding channels. Note that pressure midpoints for WT MscL (a) are higher at negative pipette voltages (asterisks), whereas V23T MscL (b) shows more symmetric responses and a more substantial shift to the left of the pressure midpoint with voltage. Plots of closed-to-open transition energy extracted from activation curves as a function of pipette voltage (c, d). Parabolic fits predict different contributions from the capacitive (quadratic) and dipole (linear) components of the dependence on potential V . Notably, both channels show ‘lingering’ conductive states at high negative voltages after stimulating pressure is released (black arrows). This behaviour was reproduced in four independent patches for each MscL version.

At the -100 mV pipette potential, the unfavourable dipole contributions constitute 1.93 and 0.53 kT and the favourable capacitive contributions are -1.35 and -3.11 kT for WT and V23T MscL, respectively. These experimentally estimated contributions raise the following questions:

(i) What is the nature of the dipole that dominates the WT MscL voltage response?

(ii) Although the V23T mutation does not change the net charge of the protein, why and how does it change the dipolar contribution?

(iii) Can the increased hydration of the V23T pore account for the large dielectric contribution in the mutant?

(iv) Where does the localized electric field exert its action in the system?

We hypothesize that MscL's dipole arises from uneven charge distribution between the cytoplasmic and periplasmic domains, but the motion of these charges in the course of gating transitions (closed \leftrightarrow expanded \leftrightarrow open) is also accompanied by an electric field re-distribution due to protein flattening and pore widening, hydration, and opening. Figure 13 visualizes the positions of charged residues and the distribution of electrostatic potential for *E. coli* MscL models in the closed and open states with charged groups in their default states at neutral pH. The computation was done with the Particle Mesh Ewald (PME) algorithm in vacuum, i.e., it reflects only the protein contribution to electrostatics, unmitigated by the medium. The color density indicates that the periplasmic side harbours the loops with the highest density of net negative charge, whereas the cytoplasmic side is richer in positive charges. These groups of charges clustered on opposite sides of the membrane form an effective dipole. We have to note, however, that all the smaller partial charges (e.g. hydroxyls), as well as the net dipole moments of the transmembrane helices, bring certain distributed contribution to the calculated net dipole moment. The transition from the closed to the open state flattens the barrel essentially bringing the charges closer, but at the same time it brings the boundaries of the applied potential over the protein barrel closer together, thus increasing the intensity of the transmembrane field. In addition, pore opening changes the distribution of electric field along the conductive pathway. The experiment (Figure 12) instructs us that negative pipette potential (on the periplasmic side) makes opening of WT MscL less favourable. This seems counterintuitive because this voltage configuration should favour a more flat, i.e. open, conformation. However, changes in electric field distribution may reverse the effect. Indeed, if we consider the positions of equipotential surfaces around the closed and (flatter) open conformations, it may become possible that the charged clusters constituting MscL's dipole become exposed to a larger fraction of the external electric field that drops across the membrane segment harbouring the channel. The taller and more 'protein-shielded' closed conformation becomes more favourable at negative pipette potentials. Our order-of-magnitude estimation shows that the observed energetic effects of the dipole component can be reasonably obtained even in simplified cylindrical representation of the channel based on the spatial and electrostatic features of the closed, expanded (subconductive), and open conformations of the homology models of WT and V23T MscL.

Table 1: major geometric parameters of the transition for WT, some dielectric properties of components, and calculated energies associated with the transitions.

		Parameter	Closed	Open
Model parameters	Ring of annular lipids	External radius of the lipid ring, nm	3.50	3.95
		Height of the periplasmic polar region, nm	1.00	1.00
		Height of the nonpolar region, nm	2.00	1.50
		Height of the cytoplasmic polar region, nm	1.00	1.00
	Protein barrel	External radius of the protein barrel, nm	2.50	2.95
		Height of the periplasmic polar region, nm	2.50	1.30
		Height of the nonpolar region, nm	2.00	1.10
		Height of the cytoplasmic polar region, nm	3.00	1.60
	Ion-conducting pore	Radius of the pore, nm	1.00	1.45
		Height of the gate region, nm	2.00	
		Height of the cytoplasmic polar region, nm	2.50	
		Height of the C-terminal bundle, nm	3.00	
	Effective dipole	Dipole moment of the channel, D	2675	2175
		Length of the channel dipole, nm	5.09	4.33
		Fraction of the dipole length in the field gradient	1.00	1.00
Fraction of the field for the negative end position		0.92	0.89	
Fraction of the field for the positive end position		0.15	0.03	
Energetic contributions, relative to the closed state	Capacitive, ring of annular lipids, kT			-0.07
	Capacitive, protein barrel, kT			-0.40
	Capacitive, ion-conducting pore, kT			-0.80
	Capacitive, access region, kT			-0.05
	Capacitive total, kT			-1.37
	Effective dipole, kT			1.98
	Total, kT			0.61

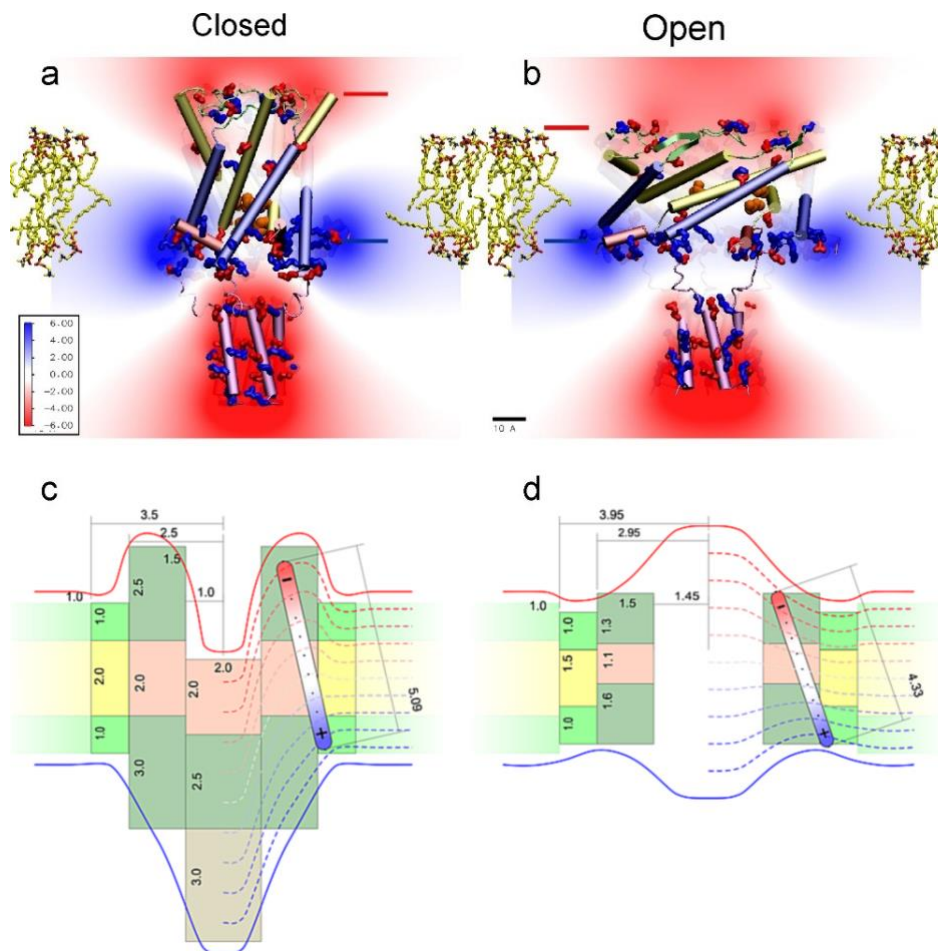


Figure 13: Estimations of WT MscL changes in dipole and capacitive energies as a result of channel opening. Distributions of electric potential around the MscL complex in the closed (a) and open (b) conformations. The density of red and blue color reflects the calculated electrostatic potential of the protein, negative to positive respectively. Cylindrical representations of the closed (c) and open (d) conformations of WT MscL. Grey and pink regions represent high-dielectric (polar) and low-dielectric (apolar) segments of the protein; green and yellow represent polar and apolar regions of the annular lipids around the protein. Numbers represent thicknesses and radii of different dielectric segments that undergo conformational changes. The red and blue lines depict equipotential surfaces around the protein and membrane, the red line designates negative voltage in the outer (periplasmic) compartment and the blue line – positive potential in the cytoplasm.

The reason for capacitive (dielectric) energy change for WT MscL is reasonably explained by the replacement of the low-dielectric pore-occluding part of the protein in the closed conformation with a volume of water in the open pore polarized by the part of the external voltage that drops across the transmembrane conductive pathway. Table 1 presents the major geometric parameters of the transition for WT, some dielectric properties of components, and calculated energies associated with the transitions.

As was concluded from the parabolic fit of data on Figure 12d, V23T MscL shows a considerably smaller dipole, but at the same time a much larger dielectric contribution than those of WT MscL. It is known that in contrast to WT, which gates mostly between the fully closed and fully open states, this mild gain-of-function mutant resides in multiple subconductive states. This means that the gate of its massively pre-hydrated and expanded pore is partially closed. Consequently, we introduce a highly populated intermediate pre-expanded (subconductive) state

in our gating scheme (Figure 14). The modelled closed state of V23T exhibits a slightly deeper water-filled external vestibule compared to WT. The expanded state has a narrow partition that separates the upper and lower compartments, which poses the main resistance and therefore essentially the entire transmembrane voltage drops across this narrow part. We should mention that this partition may contain a large fraction of solvating water and thus must have a high-dielectric property, being also somewhat leaky for ions. This narrow region where most of the voltage drops will be characterized by high capacitive energy and thus will be strongly favoured by voltage. The transition to the fully open state redistributes voltage in that region, which now smoothly drops across the entire length of the pore including adjacent regions of aqueous solution posing access resistances to the pore. Effective parameters of the system that readily account for dielectric contributions of different states are presented in Table 2.

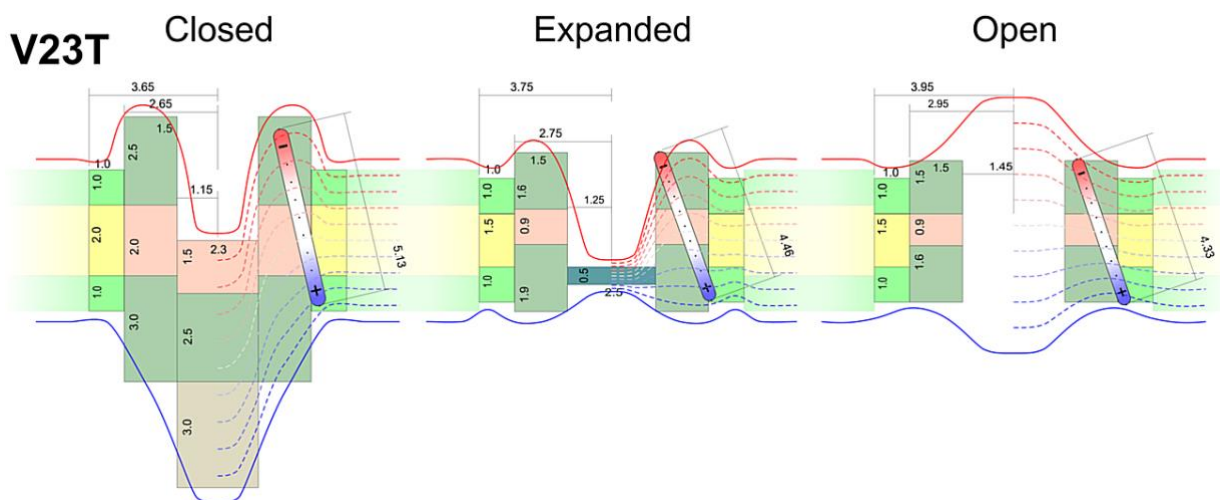


Figure 14: Cylindrical representations of three main conformations of V23T MscL, closed, expanded and open. Grey and pink regions represent high-dielectric (polar) and low-dielectric (apolar) segments of the protein; cyan domain in the expanded state shows polar hydrated occlusion of subconductive pore; green and yellow represent polar and apolar regions of the annular lipids around the protein. Numbers represent thicknesses and diameters of different dielectric segments that undergo conformational changes. The red and blue lines depict equipotential surfaces around the protein and membrane, in this particular case red line designates negative voltage in the outer (periplasmic) compartment.

It is important that the highly populated intermediate state, with a wide fully hydrated outer vestibule, permits free ion passage into the water-filled cavity that concentrates the field on a narrow partition. As a result, there is considerably less voltage dropping across the whole protein and across the domains constituting the dipole. In addition, the periplasmic part of the protein in this model is not yet as flattened as in the fully open state, which keeps the potential boundary at a larger distance from the positive (cytoplasmic) end of the effective dipole. For these reasons, the dipole contribution in V23T is about 6 times less compared to WT. The key parameters for estimations are presented in Table 2.

Table 2: Parameter estimations for dipole calculations.

		Parameter	Closed	Expanded	Open	Effective "conductive"	
Model parameters	Ring of annular lipids	External radius of the lipid ring, nm	3.65	3.75	3.95		
		Height of the periplasmic polar region, nm	1.00	1.00	1.00		
		Height of the nonpolar region, nm	2.00	1.50	1.50		
		Height of the cytoplasmic polar region, nm	1.00	1.00	1.00		
	Protein barrel	External radius of the protein barrel, nm	2.65	2.75	2.95		
		Height of the periplasmic polar region, nm	2.70	1.60	1.50		
		Height of the nonpolar region, nm	1.80	0.90	0.90		
		Height of the cytoplasmic polar region, nm	3.00	1.90	1.60		
	Ion-conducting pore	Radius of the pore, nm	1.15	1.25	1.45		
		Height of the gate region, nm	2.70	0.50			
		Height of the cytoplasmic polar region, nm	1.80				
		Height of the C-terminal bundle, nm	3.00				
	Effective dipole	Dipole moment of the channel, D	2675	2175	2175		
		Length of the channel dipole, nm	5.13	4.46	4.33		
Fraction of the dipole length in the field gradient		1.00	0,9	1.00			
Fraction of the field for the negative end position		0.92	1.00	0.89			
Fraction of the field for the positive end position		0.15	0.12	0.03			
Energetic contributions,	Capacitive, ring of annular lipids, kT			-0.05	-0.07	-0.06	
	Capacitive, protein barrel, kT			-0.32	-0.43	-0.37	
	Capacitive, ion-conducting pore, kT			-4.64	-0.79	-2.71	
	Capacitive, access region, kT			0.03	-0.01	0.01	
	Capacitive total, kT			-4.94	-1.30	-3.12	
	Effective dipole, kT				-1.11	2.21	0.55
	Total, kT				-6.05	0.91	-2.57

Tests for local field effects

The energy of MscL gating transition is affected by an externally applied electric field. For V23T MscL the effect is especially strong because the geometric shape of this pre-hydrated channel in expanded states (highly populated in V23T) permits ion penetration into the vestibule which concentrates the electric field on a relatively narrow well-hydrated (and therefore polarizable) region. The voltage-dependence of V23T MscL is therefore likely imparted by a highly localized electric field. To test this notion and to answer the question of whether the inner electric field that drops inside the membrane matters more than the externally imposed voltage, we studied

voltage-dependent gating of V23T MscL in asymmetric DIBs characterized by a constant electrostatic bias created by the difference of interfacial dipole potentials of two lipid leaflets and compared the results with symmetric DIBs (see Figure 15).

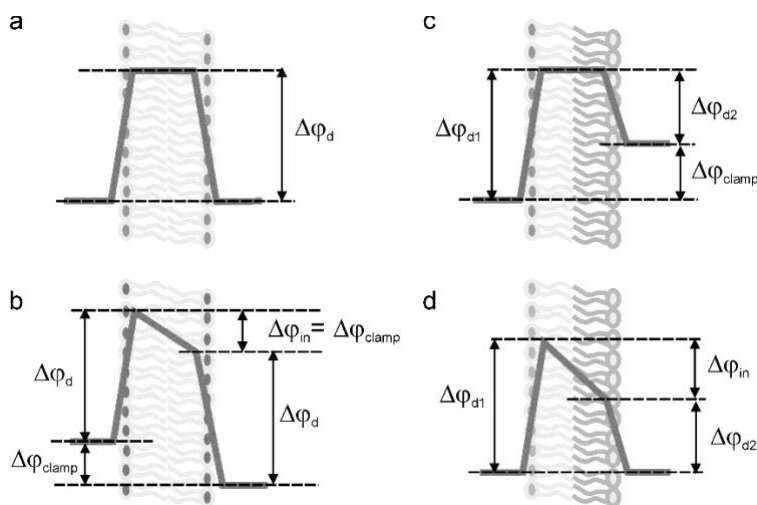


Figure 15: Electric field distribution across electrically neutral symmetric (a, b) and asymmetric (c, d) membranes composed of two leaflets characterized by different surface dipole potentials.

The directionally reconstituted V23T MscL shows voltage dependence in symmetric membranes.

In an effort to replicate the results from the recordings in native patches, we asymmetrically incorporated V23T MscL in a DIB system by introducing the channels unilaterally, only in the droplet connected to the ground. An external potential of 100 mV was applied while the droplets were mechanically stimulated at 0.2 Hz and by using different duty cycles in order to control the tension in the bilayer. The polarity of the applied potential was flipped repeatedly while recording the current. In agreement with the native patches' findings, V23T MscL gated only at the potentials above 80 mV and exhibited higher activity in the presence of a negative potential (Figure 16b,e). In addition, both the opening probability per cycle and the conductance of the substates were higher (Figure 16c, f). At both voltages we observed very few full openings, however, more high-conductive substates were occupied when a negative potential was applied when compared to positive potentials. Upon application of positive potentials, low-conductive substates were occupied while none of the fully open states were observed. (It is also worth mentioning that the open dwell time at positive potentials was shorter compared to negative potentials.

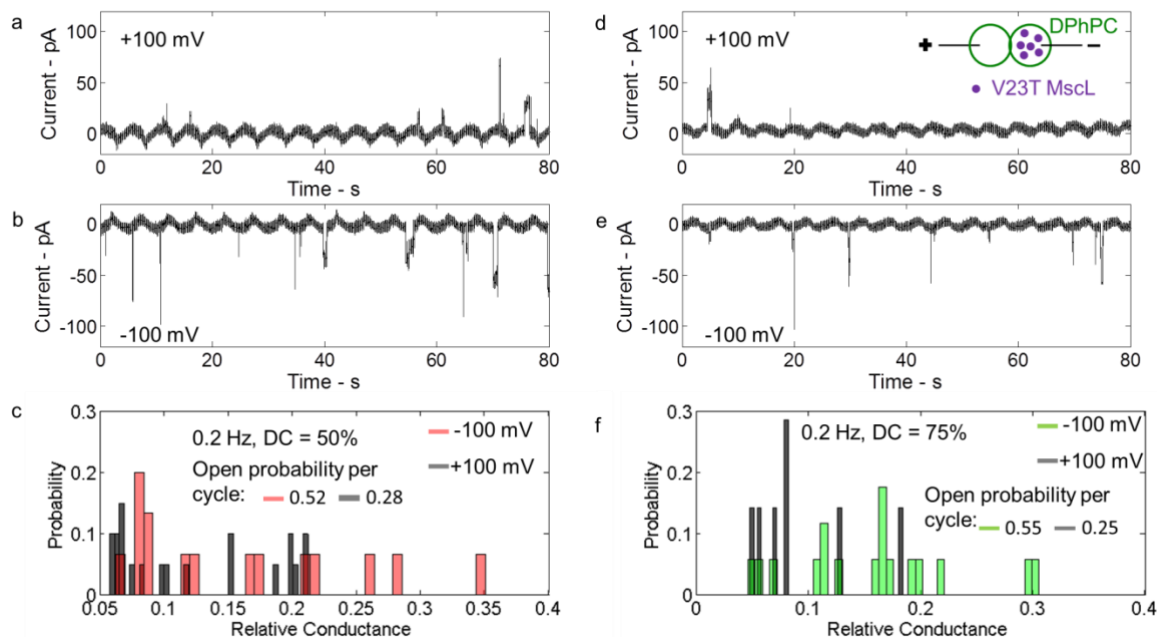


Figure 16: The gating behaviour of V23T when incorporated asymmetrically in a symmetric DPhPC bilayer. The droplets were oscillated at 0.2 Hz with duty cycles of 50% (a-c) and 75% (d-f) (it was demonstrated in a separate study that higher duty cycle values create higher bilayer tension), while an external transmembrane potential of 100mV was applied. The voltage polarity is repeatedly switched, (and similar to the results in native patches), the channels exhibited higher activity in the presence of a negative potential (b and e), while at positive potential a few sub-conductive events are observed (a and b). Amplitude histograms of V23T MscL opening events obtained from multiple traces are presented in (c and f). At both duty cycles, V23T MscL exhibits higher open probability as well as higher conductance substates in the presence of negative potentials.

Effects of membrane asymmetry

V23T MscL asymmetrically incorporated within an asymmetric bilayer (Figure 17) displays a higher activity upon the application of negative external potentials, which will add to the already existing negative intrinsic bias caused by membrane asymmetry (Figure 17a,c). However, the most interesting and significant finding was irresponsiveness of V23T MscL in the presence of a positive 100 mV external potential (Figure 17d). The application of a positive 100mV counterbalances the already existing -130mV and diminishes its contribution to a -30 mV (the sum of both the externally applied voltage and the intrinsic bias), a value proven insufficient for the activation of V23T MscL in DIBs.

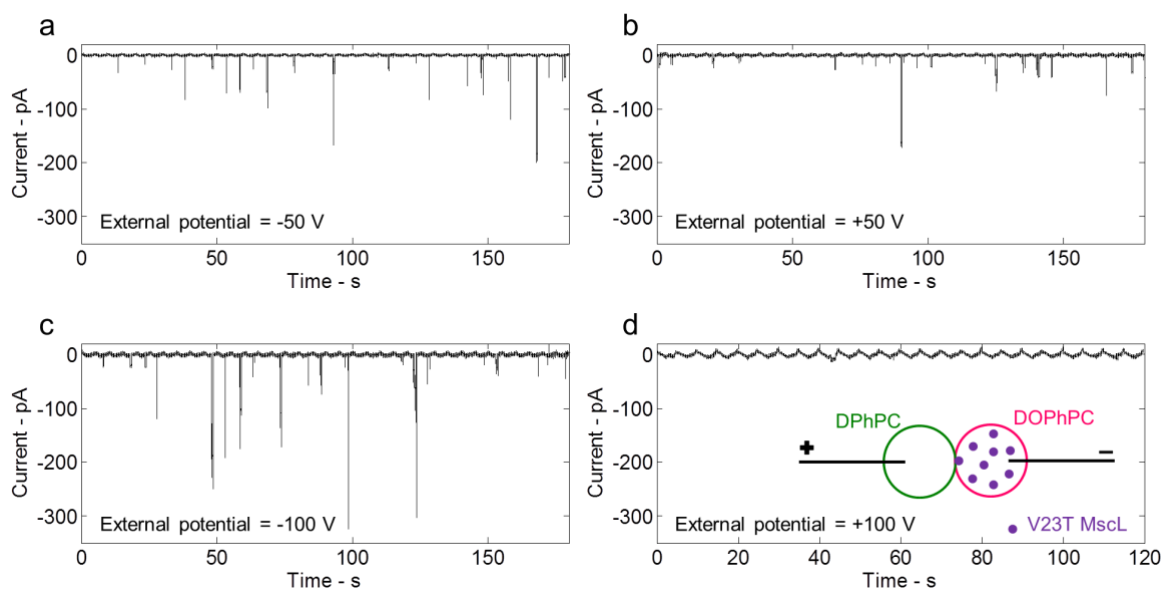


Figure 17: V23T MscL channels asymmetrically incorporated within asymmetric bilayers exhibit strong voltage-dependency. (a) The channels were introduced to the droplet containing DOPhPC and connected to the ground. At the membrane, the intrinsic potential bias is equal to -130 mV, the application of a -50 mV external potential lead to a -180 mV transmembrane potential, causing high V23T MscL activity. (b) Switching the external potential to +50mV lead to a -80mV potential across the membrane, which caused gating, however, mostly lower conductance sub-states in comparison with the previous case. (c) At -100mV, V23T MscL is highly active and several fully open states and high conductance sub-states. (d) V23T MscL exhibits no activity when subjected to a positive 100mV, a value that would counterbalance and limit the effect of the intrinsic electric bias, strongly establishing the voltage dependency of the V23T mutant of MscL.

Conclusions

V23T MscL, the mild gain-of-function mutant of the bacterial mechanosensitive valve MscL, is a promising tension sensor that can be used in bio-inspired materials engineering not only because it gates at lower tension levels but also because it features a considerably stronger modulation by voltage.

Like WT MscL, V23T possesses both components of voltage-sensitivity, the linear (dipole-related) component and the quadratic (dielectric) component. The linear component slightly favors opening at hyperpolarizing voltages visible at positive pipette potentials in patch-clamp experiments and in a specific configuration in DIBs with directionally reconstituted V23T MscLs.

The stronger dielectric component of voltage sensitivity of V23T MscL originates from the non-specific capacitive effect of high-dielectric water that displaces the protein when the channel expands in its semi-open (subconductive) state, i.e., in the constricted region specifically subjected to the strong electric field. The estimations show that the observed dielectric energy contributions are in good agreement with the volume of polarized water pulled into the pore constriction and with geometric adjustments of the surrounding protein and annular lipids.

Energies of specific states strongly depend on the electric field configuration around the channel, which in turn depends on pore conductance and channel reshaping.

The dielectric effect on V23T gating is governed by the local electric field dropping in the vicinity of the channel gate, including the part inside the membrane. Here we show that V23T gating is strongly modulated by dipole potentials in the interfacial layers of the membrane. This effect observed in asymmetric DIBs demonstrates that DIBs is a convenient experimental system allowing for control of individual surfaces of the artificial membrane.

3. Coupling of multiscale models to macroscale models that enable the design of biomolecular materials for sensing, actuation, and energy conversation.

One of the compelling features of biomolecular networks is the ability to incorporate stimuli-responsive biomolecules in the interfacial bilayer. Several demonstrations of the functionality of such systems have been shown by multiple researchers. These networks typically incorporate multiple droplets with or without embedded biomolecules that shape the response of the system to various external stimuli as seen in Figure 18.

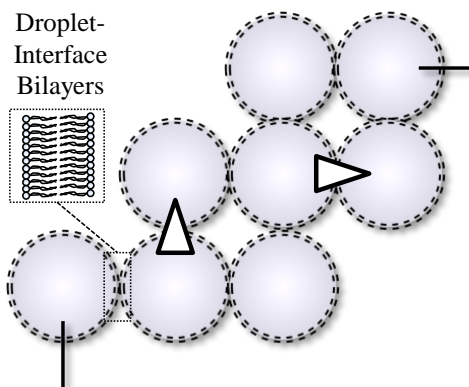


Figure 18 - Illustration of an envisioned biomolecular networks. Multiple droplets with or without embedded stimuli-responsive biomolecules allow for advanced material responses to various stimuli.

In this program we developed a deterministic model of these envisioned biomolecular networks is developed that may be used to predict the behavior of these coupled bilayer-biomolecules systems. Such a model will prove useful for the design of biomolecular sensing systems that incorporate stimuli-responsive biomolecules such as peptides and proteins. This paper focuses on the development of deterministic models of network properties that simulates the passive properties of the networks as well as the properties are derived from the behavior of stimuli-responsive biomolecules incorporated into the interfacial bilayers.

Biomolecular Network Modeling

The goal of the modeling effort is to develop mathematical representations of bilayer networks that are functions of both the bilayer properties and the properties of the surrounding aqueous phases. To this end, a revised form of the Hodgkin-Huxley model is considered which combines the imperfect capacitance circuit properties of the lipid bilayer with the conductance of the surrounding aqueous phases. For simplicity, the variable α is defined as the ratio of the conductance of the aqueous phases (G_f) over the conductance of the bilayers (G_b). The four-node model is illustrated in Figure 19.

This model approximates the bilayer as a capacitance element with a capacitance value of C_b in parallel with a conductor with a conductance value of G_b . A voltage-dependent biomolecule term is inserted in parallel through the function $P_b(V)$, which allows for the simulation of voltage-dependent protein and peptide activity such as voltage-gated channels. Finally, the surrounding aqueous phase contained inside of the droplets is approximated through conductors

defined by αG_b , where α is the ratio of the fluid conductance to the bilayer conductance (G_f/G_b). Since the bilayer response is highly dependent on this ratio α it will be used in future discussions. Recall that αG_b is equivalent to G_f , or the conductivity of the fluid.

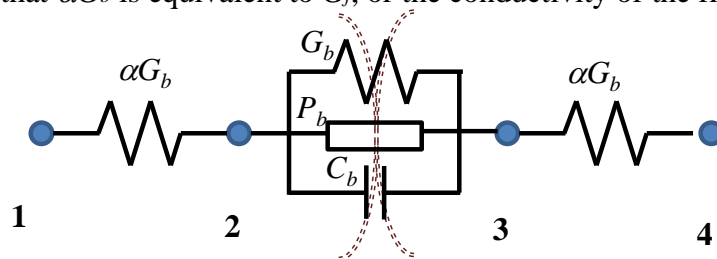


Figure 19: Electrical circuit representation of the bilayer unit cell. The bilayer conductance is represented as G_b , the bilayer capacitance is represented as C_b , the biomolecule conductance as P_b , and the aqueous phase conductance is represented as a ratio of the bilayer conductance through αG_b .

This proposed electrical system may be represented as a four-node element through nodal voltage analysis. From Kirchoff's Current Law (KCL) applied at the nodes in Figure 19, the state equations for this unit cell model are derived as:

$$\begin{bmatrix} 0 & 0 & 0 & 0 \\ 0 & C_b & -C_b & 0 \\ 0 & -C_b & C_b & 0 \\ 0 & 0 & 0 & 0 \end{bmatrix} \begin{bmatrix} \dot{v}_1 \\ \dot{v}_2 \\ \dot{v}_3 \\ \dot{v}_4 \end{bmatrix} + \begin{bmatrix} \alpha G_b & -\alpha G_b & 0 & 0 \\ -\alpha G_b & \alpha G_b + G_b & -G_b & 0 \\ 0 & -G_b & G_b + \alpha G_b & -\alpha G_b \\ 0 & 0 & -\alpha G_b & \alpha G_b \end{bmatrix} \begin{bmatrix} v_1 \\ v_2 \\ v_3 \\ v_4 \end{bmatrix} + \begin{bmatrix} 0 & 0 & 0 & 0 \\ 0 & P_b & -P_b & 0 \\ 0 & -P_b & P_b & 0 \\ 0 & 0 & 0 & 0 \end{bmatrix} \begin{bmatrix} v_1 \\ v_2 \\ v_3 \\ v_4 \end{bmatrix} = \begin{bmatrix} 0 \\ 0 \\ 0 \\ 0 \end{bmatrix} \quad (1)$$

which provides the relationships between each of the nodes depicted in Figure 19. We refer to Equation (1) as the four-node unit cell model as it encompasses all four nodes contained in the electrical circuit representation of the bilayer. The three matrices that comprise the model are the unit cell bilayer capacitance matrix \mathbf{c} , bilayer/fluid conductance matrix \mathbf{g} , and stimuli-responsive biomolecule conductance matrix \mathbf{p} . The capacitance matrix of the four-node unit cell model is singular, arising from the fact that there are no capacitive elements crossing the aqueous phase elements. Therefore, this model results in a system of differential algebraic equations (DAE) which will require special considerations to solve.

Accordingly, a second model is developed that incorporates a model of the bilayer membrane but omits the conductance elements across the aqueous phase elements. The unit cell equation for this model may be seen in Equation (2). This assumption is based on the low conductance of the bilayer (typically on the order of 10^{-12} S for the systems studied here that do not contain conductive biomolecules) allowing for negligible contribution from the conductive fluid elements at low frequencies. This assumption allows for a non-singular capacitance matrix through directly connected bilayer elements.

$$\begin{bmatrix} C_b & -C_b \\ -C_b & C_b \end{bmatrix} \begin{bmatrix} \dot{v}_1 \\ \dot{v}_2 \end{bmatrix} + \begin{bmatrix} G_b & -G_b \\ -G_b & G_b \end{bmatrix} \begin{bmatrix} v_1 \\ v_2 \end{bmatrix} + \begin{bmatrix} P_b & -P_b \\ -P_b & P_b \end{bmatrix} \begin{bmatrix} v_1 \\ v_2 \end{bmatrix} = \begin{bmatrix} 0 \\ 0 \end{bmatrix} \quad (2)$$

For both cases, the state equations may be combined to form larger matrices that dictate the behavior of collections of bilayers. This requires use of the transformation matrix λ , which transcribes the coefficient matrices from either of the two bilayer stencils to larger systems containing multiple bilayers as seen in Equation (3),

$$\begin{aligned} \mathbf{G} &= \lambda^T \mathbf{g} \lambda \\ \mathbf{C} &= \lambda^T \mathbf{c} \lambda \\ \mathbf{P} &= \lambda^T \mathbf{p} \lambda \end{aligned} \quad (3)$$

λ is a $n \times 4$ or a $n \times 2$ matrix dependent on the selected model (Equation (1) or (2)), where n is the number of nodes present in the system. The matrices describing the total system response are then obtained by summing up each of the transcribed matrices from Equation (3) as seen in Equation (4).

$$\begin{aligned} \mathbf{G}_{sys} &= \sum_1^n \mathbf{G}_n \\ \mathbf{C}_{sys} &= \sum_1^n \mathbf{C}_n \\ \mathbf{P}_{sys} &= \sum_1^n \mathbf{P}_n \end{aligned} \quad (4)$$

Now that the total system property matrices have been created, they may be used again to describe the behavior of the system as seen in Equation (5).

$$\mathbf{C}_{sys} \bar{\dot{V}} + \mathbf{G}_{sys} \bar{V} + \mathbf{P}_{sys} \bar{V} = \bar{0} \quad (5)$$

These equations provide a passive response for node-to-node relationships. Since the systems considered in the laboratory are studied using patch-clamp approaches, appropriate boundary conditions are applied by setting two nodes equal to the source voltage and the ground. These nodes are then set to fixed values or functions. The source node is typically set equal to a sinusoidal input $A \sin(\omega t)$ and the ground node is set to 0 mV. This provides the information for the right hand side of Equations (1) through (5), and the response of the nodal voltages to these prescribed boundary conditions may be studied.

System Passive Response Analysis

The complete four node model results in a system of differential algebraic equations which require specialized methods for their solution. The method selected for the solution of the four-node model involves the application of Laplace transforms where the governing equation becomes:

$$\mathbf{C}_{sys} \bar{V} s + \mathbf{G}_{sys} \bar{V} + \mathbf{P}_{sys} \bar{V} = F(s) \quad (6)$$

where s is the traditional Laplace variable in the s domain, and $F(s)$ is the transformed voltage input from the boundary conditions.

To find a closed-form tractable solution, the stimuli-responsive biomolecule conductance matrix \mathbf{P}_{sys} must be omitted from the system as the coefficients are typically expressed as functions of the voltage differences across the bilayer elements (or membrane potentials). Therefore, this Laplace method is suitable for examining the passive response of the bilayer network with an applied voltage, but a different solution method will be required for studying the impact of voltage-dependent channels. Algebraically solving the system of equations from Equation (6) generates transfer functions for the ratio of the voltage at the internal nodes V_i (where i corresponds to the selected node number from 1 to n as seen in Figure 20) to the source node V_s which then may be converted back to the time-dependent solution through inverse Laplace transformations. An example of the solution obtained from this approach may be seen in Figure 20 for a three-unit cell system as indicated in the bottom right corner of the figure.

For the simulations presented in this section, baseline parameters are employed. The capacitance is assumed to be 500 pF for both bilayers, the conductance of both bilayers is assumed to be 1 pS, the input forcing function is a sinusoidal 150 mV potential at a variable frequency, and the aqueous conductance is assumed to be 1 μS yielding a value of 106 for α .

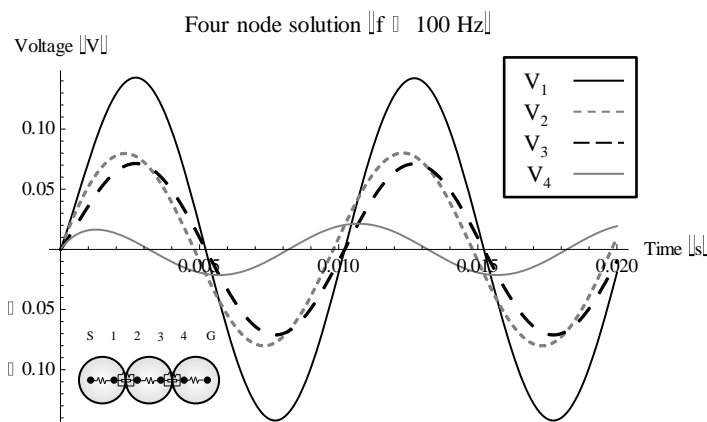


Figure 20: Four node analytical solution obtained through Laplace transformations for a three droplet / two unit cell system with a sinusoidal voltage input (amplitude 0.15 V, frequency 100 Hz) applied at node S and a ground at node G.

This Laplace approach allows for the rapid solution of linear chains of bilayer unit cells (Figure 21). Several of these chains with varying lengths were constructed and the results were compared. If the properties of each unit cell (G_b , C_b , α) remain constant throughout the chain then a series of simplifications occurs in the voltage transfer functions (V_i/V_s) due to pole-zero cancellations. This results in a pattern for the transfer functions that may be extended to infinite bilayer chains. Equations (7) and (8) predict the transfer function for node i relative to the source voltage V_s in a linear droplet chain of length n (where i ranges from 1 to n). For further simplicity, a time variable τ_n is defined as the frequency at which the low-pass filter behavior of the bilayer occurs. This variable is adjusted dependent on the length of the chain, and corresponds to the inverse of the remaining pole of the transfer functions (Equation (7)). Independent of the length of the bilayer unit cell chain, the transfer functions each contain this one single pole as long as the properties of each unit cell are uniform.

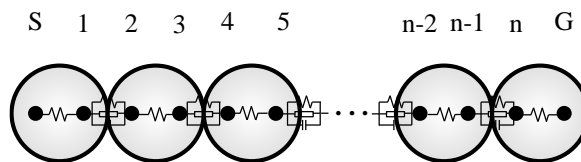


Figure 21 - Linear chain of droplets of length n . The source is labeled as S , the ground as G .

$$\tau_n = \frac{(n+2)Cb}{2\pi(n+2+n\alpha)Gb} \quad (7)$$

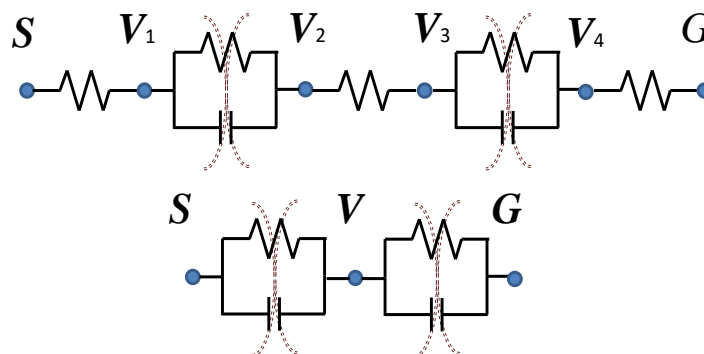
$$\frac{V_i}{V_s} = \begin{cases} \frac{\frac{(1+\alpha)(n+1-i)}{n+2+n\alpha} + \frac{n+1-i}{n+2} 2\pi s\tau}{1+2\pi s\tau} & i = 1, 3, 5, 7 \dots \\ \frac{\frac{(n+2-i+(n-i)\alpha)}{n+2+n\alpha} + \frac{n+2-i}{n+2} 2\pi s\tau}{1+2\pi s\tau} & i = 2, 4, 6, 8 \dots \end{cases} \quad (8)$$

Solving for the time-domain solution reveals that the voltage response exhibits three behaviors. At low frequencies the voltage drop is dominated by the bilayer elements. As the frequency of the applied signal at the source node V_s increases, the voltage drop begins to occur across both the bilayer elements and the connecting aqueous conductors. Once the frequency increases to a sufficient level, the voltage drop is dominated by the aqueous phase elements, causing the voltage drop observed by the bilayers to diminish. This results in a reduction in the membrane potential that is often crucial for the stimuli-responsive biomolecules present in the bilayer. This is indicative of the droplet length (and consequently resistance) becoming too great for the mobile ions carrying the signal to fully distribute across the droplet volume in the time allowed, resulting in a potential drop between the opposite ends of the droplet rather than across the bilayers.

As this Laplace transformation method does not allow for voltage dependent biomolecule function, the two-node simplification may be employed for further studies. This allows for the application of traditional numerical techniques solving the systems of ODEs, but first the range of validity for the two-node simplification must be determined.

This range of validity for the two-node solution is examined through the following case study. A three droplet – two-unit cell system is constructed as seen in Figure 22 with three aqueous phases

and two bilayers. The input is applied at node S and the ground is set to node G for both solution



methods.

Figure 22 - Comparison of the four node (top) and two node (bottom) model for a three droplet / two unit cell system. Inputs are applied at node S, and the ground is set to node G.

The low-pass filter behavior may be studied by plotting the impedance of both the two node and the four-node system across a single bilayer, where the admittance is calculated as:

$$Y_{4node} = \frac{G_b \alpha (G_b + j\omega C_b)}{G_b \alpha + 2G_b + 2j\omega C_b} \quad (9)$$

$$Y_{2node} = G_b + j\omega C_b \quad (10)$$

The magnitude of the admittance and the angle are plotted in Figure 23b. These figures are plotted with respect to the RC frequency constant f_c , which is given by Equation (11). The conductivity ratio α for these plots is set to 10^6 .

$$f_c = \frac{G_b}{2\pi C_b} \quad (11)$$

These plots demonstrate that the four node and the two-node solution diverge at higher frequencies as marked in Figure 23b by the vertical dashed line. From the phase angle plot, the divergence occurs when:

$$f \geq \frac{G_b}{2\pi C_b} 10^{\left(\frac{\text{Log}_{10}(\alpha)}{2}\right)} \quad (12)$$

For the baseline case ($C_b = 500$ pF, $G_b = 1$ pS, $\alpha = 10^6$, no proteins), this corresponds to a divergence frequency of 0.32 Hz for the four node and two node solutions. This cutoff point is marked by a vertical dashed line in Figure 23b. It should be noted that this cutoff point aligns with the point at which the solutions begin to diverge for a single bilayer. This divergence is initially minimal, and no meaningful difference is observed until 100 Hz. However, this threshold still provides a definite point at which the two solutions are guaranteed to remain equivalent. This threshold frequency defined in equation (12) allows the researcher to determine which solution method is appropriate for their biomolecular system.

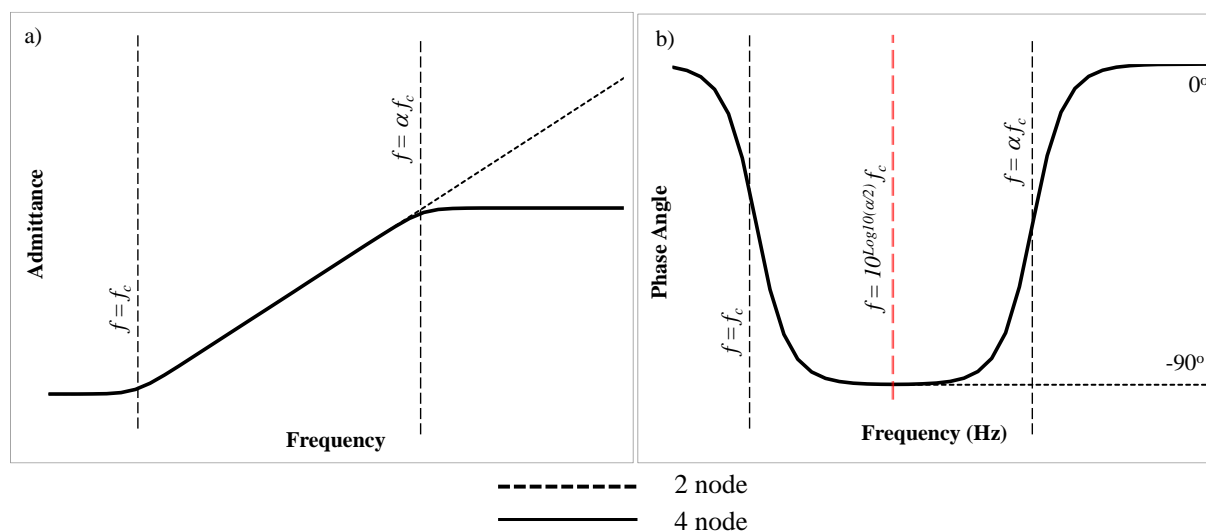


Figure 23 – a) Admittance magnitude and b) phase angle plots comparing the four node and two node solutions

The key difference between two solutions is their divergence at higher frequencies. This is due to the two node solution's inability to capture the voltage drop occurring across the fluid elements rather than the capacitance elements as indicated in Figure 23. The four-node model is able to account for voltage drops across these droplet interiors, which may be visualized as ion accumulation on opposite ends of the droplets leading to the development of a potential. Further analysis of this voltage shift effect may be conducted by altering the system parameters and examining the analytical solutions for both the four node and the two node models. From comparing Equation (9) and Equation (10), the two node system is equivalent to the four node system when $\alpha \rightarrow \infty$. This conductivity ratio will be varied and solutions will be plotted to test this observation.

The two-node system assumes that the aqueous phases remain infinitely conductive, ensuring that the voltage drop across these elements remains zero for all input frequencies. For a further analysis of the requirements for this two-node assumption to remain valid, the Laplace approach for the four-node solution will be employed and the analytical solution's dependence on the value of α will be examined. First, the peak voltage for each node is plotted while varying α from 1 to 10^{10} . As $\alpha \rightarrow \infty$, the two node and four node solutions converge for all frequencies as seen in Figure 24. The regions of the plot where V_2 is not equal to V_3 are the regions where the voltage drops occur across the droplet interiors rather than the bilayer elements. As the frequency is decreased or the conductance of the droplet interiors is increased, V_2 and V_3 converge and match the two-node solution at the center of the plot.

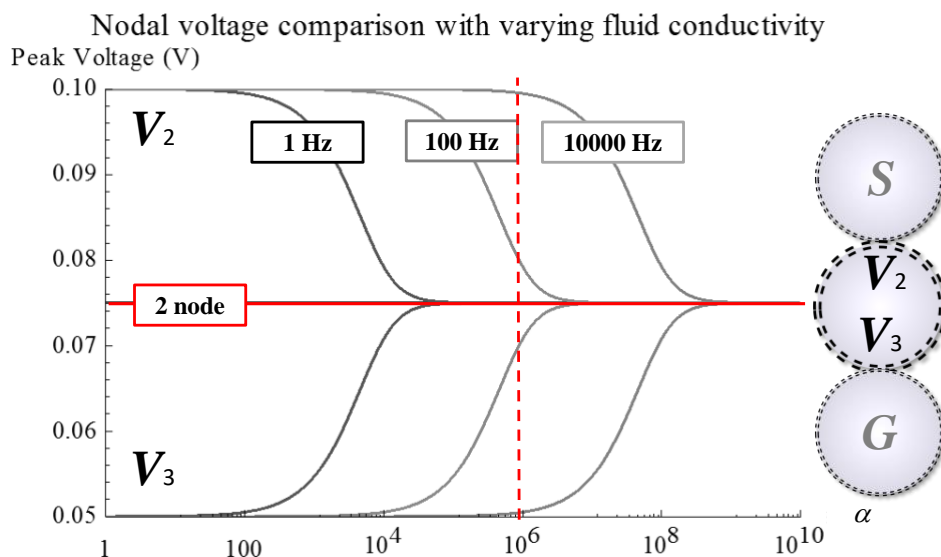


Figure 24 - Central nodal voltage comparison (nodes 2 and 3 for the four node solution, node 2 for the two node solution) with varying fluid conductivity. The two node solution for the central node is represented by the center line, and the four node solutions for nodes 2 and 3 are the upper and lower lines respectively. As $\alpha \rightarrow \infty$, the four node and two node solutions converge. The vertical dashed line represents the baseline ratio for the conductivities (106). Voltages are measured with respect to the ground G.

The results from Figure 24 show that as the operating frequency is reduced, the value for α at which the four node and two node solutions converge is similarly reduced. From these results it is apparent that the two-node solution is equivalent to the complete four node solution when the system is operated at low frequencies or when the surrounding aqueous phase is highly conductive. Ultimately the threshold frequency for the use of the two node model may be determined by Equation (12), but the authors recognize that the amount of error may remain negligible until higher frequencies are reached as indicated by Figure 24.

Natural cellular systems are able to transduce at much higher frequencies than the ones exhibited by the artificial cellular systems considered here. This is partially due to the difference between the droplet dimensions and standard cellular dimensions. The droplets considered here typically have a radius of 0.1 – 1.0 mm, and ongoing efforts aim to reduce these dimensions further. For comparison, a cellular radius is often on the order of 1-10 μm , resulting in a ratio between the natural and artificial cases of roughly 100. Rewriting Equation (12) with dependencies on this characteristic length r , and substituting $\alpha = G_f/G_b$ yields Equation (13):

$$f \geq \frac{G_b(r^2)}{2\pi C_b(r^2)} 10^{\frac{1}{2} \text{Log}_{10} \left(\frac{G_f \left(\frac{1}{r} \right)}{G_b(r^2)} \right)} \quad (13)$$

where G_b and C_b both increase with the surface area of the bilayer (r^2), and G_f decreases with the radius of the droplet (r). From this, the ratio of 1 to 100 for droplet radius to a cellular radius increases the threshold frequency by a factor of 10^3 . This threshold frequency may be radically

increased by reducing the dimensions of the droplets, providing a target for future experimental recreation.

Moving forward, the two-node simplification will be combined with biomolecule conductance behavior to provide a coupled bilayer - biomolecule model. This system will be solved using standard numerical methods as the capacitance matrix is no longer necessarily singular.

SYSTEM SIMULATIONS INCLUDING BIOMOLECULE CONDUCTANCE

The end goal of this work is to combine the primary network model with a secondary voltage-dependent biomolecule model. This secondary model for predicting the behavior of the voltage-dependent biomolecules is developed in the following section. The two-node network model will then be combined with the biomolecule model for the final coupled results.

For the voltage-dependent biomolecule, the pore α HL is considered. α HL is a self-assembling toxin from the bacteria *Staphylococcus aureus* and forms a pore when inserted into a lipid bilayer. The wild-type β -barrel pore is weakly rectifying and weakly anion selective. The engineered derivative is designed to provide a pore that is strongly rectifying and appears as the biological equivalent of the diode. Protein engineering is a relatively new field where proteins are either designed from scratch or natural proteins are changed to have a new functionality. Amino acid sequences are identified that may provide the desired function or structural properties and are used to “design” the protein. Designing a protein from scratch is more challenging because the structural backbone of the protein may not be “designable” because of uncertainty in the structural folds. In the modified protein considered for use here the protein pore α HL is used to maintain the backbone of the protein and seven residues of the protein are replaced with the amino acid arginine creating an engineered α HL protein (7R- α HL) pore. This change introduces 49 additional positively charged side chains in the barrel of the protein. The application of negative potential on the engineered protein causes a structural change in the protein or “collapse of the β barrel”. The 7R- α HL protein is strongly rectifying but has a time delay which is probably caused by the time to complete the structural change.

The ion current/membrane potential relationship of the engineered 7R- α HL protein is graphically presented from measurements taken in a Droplet-Interface Bilayer (DIB) consisting of DPhPC lipids with the two aqueous solutions consisting of 1 M KCl, 25 mM Tris HCl at pH 8.0 and 100 μ M of the protein. The graph shows the ion current/membrane potential relationship for different instances of time where one plot is for the instantaneous time after a potential increase and the other plot is for the steady-state time. The instantaneous relationship refers to the ion current/membrane potential relationship directly after a step to that specific potential. Therefore, the conformational structure change of the 7R- α HL pore to negative potential has not occurred. The steady-state (ss) relationship refers to the ion current/membrane potential relationship after the conformational structure change has occurred. As discussed, there is time dependence in the conformation change of the protein barrel when a negative membrane potential is applied. This distinction between the steady-state and instantaneous relationship highlights the extremes of the time dependence. The instantaneous and steady state relationships caused by positive membrane potentials are equal. A least square fit is used to obtain an analytical expression for the ion current/membrane potential relationship for the instantaneous relationship. The fit is forced to pass through the origin. The steady-state ion current/membrane

potential relationship for a positive applied potential is the same as for the instantaneous relationship and the conductance with a positive potential is the slope of the fit. The conductance of the steady-state relationship for a negative applied potential is zero. Figure 25b shows plots of the conductance (G_p) comparing the steady state and the instantaneous relationships.

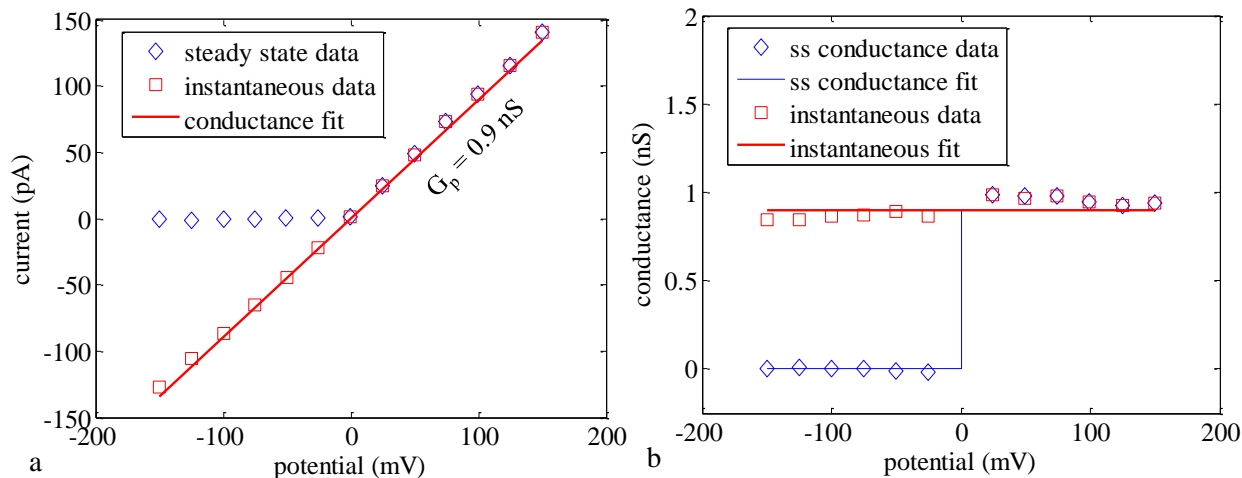


Figure 25 - a) Current/membrane potential relationship of 7R- α HL in steady state and with instantaneous potential changes with a least square fit of the data and b) the conductance of the data of 7R- α HL for the steady state and instantaneous cases.

The measured ion current between the instantaneous and the steady state cases is reported to follow two double exponential decays with time constants of 210 ms and 1.0 s [15]. The decay dynamics are included in the conductance model to simulate these time variations between the instantaneous and steady state cases. This decay is included in Equation (14) where the instantaneous conductivity is:

$$P = \begin{cases} m, & \text{if } V \geq 0 \\ \frac{m}{2} \left(e^{-\tau_1 t(0)} + e^{-\tau_2 t(0)} \right), & \text{if } V < 0 \end{cases} \quad (14)$$

where m is the conductance of the instantaneous case, τ_1 is the inverse of the smaller decay constant, τ_2 is the inverse of the larger decay constant, and t is a time vector that starts at zero for every instance when the membrane potential changes from a positive value to a negative value. The steady-state conductance values are calculated in a similar piecewise fashion through Equation (15).

$$P = \begin{cases} m, & \text{if } V \geq 0 \\ 0, & \text{if } V < 0 \end{cases} \quad (15)$$

These equations mirror the behavior of the protein shown in Figure 25b and provide the approximate conductance decay reported for the negative membrane potentials associated with the protein.

COUPLED SYSTEM RESULTS

The coupled two node network model and the protein conductance model are now combined to study behavior of systems of multiple bilayers with inserted proteins. For comparison, an experimental case is used as shown in Figure 26. The system contains four droplets with connective bilayers. 7R- α HL proteins are oriented in each bilayer as shown in the schematic by the diode illustrations. This system offers the possibility of full-wave rectification, altering a triangle voltage waveform to a constantly positive current output.

Following the network modeling procedures and applying the potential at droplet 2 and setting the ground to droplet 3, the equations for solving the membrane potentials are:

$$\begin{aligned} \begin{bmatrix} \dot{V}_1 \\ \dot{V}_2 \\ \dot{V}_4 \end{bmatrix} &= \begin{bmatrix} C_{12} + C_{13} & -C_{12} & 0 \\ -C_{12} & C_{12} + C_{24} & -C_{24} \\ 0 & -C_{24} & C_{24} + C_{34} \end{bmatrix}^{-1} \begin{bmatrix} -(G_{12} + G_{13}) & G_{12} & 0 \\ G_{12} & -(G_{12} + G_{24}) & G_{24} \\ 0 & G_{24} & -(G_{24} + G_{34}) \end{bmatrix} \begin{bmatrix} V_1 \\ V_2 \\ V_4 \end{bmatrix} \\ &+ \begin{bmatrix} C_{12} + C_{13} & -C_{12} & 0 \\ -C_{12} & C_{12} + C_{24} & -C_{24} \\ 0 & -C_{24} & C_{24} + C_{34} \end{bmatrix}^{-1} \begin{bmatrix} -(P_{12} + P_{13}) & P_{12} & 0 \\ P_{12} & -(P_{12} + P_{24}) & P_{24} \\ 0 & P_{24} & -(P_{24} + P_{34}) \end{bmatrix} \begin{bmatrix} V_1 \\ V_2 \\ V_4 \end{bmatrix} \\ &+ \begin{bmatrix} C_{12} + C_{13} & -C_{12} & 0 \\ -C_{12} & C_{12} + C_{24} & -C_{24} \\ 0 & -C_{24} & C_{24} + C_{34} \end{bmatrix}^{-1} \begin{bmatrix} 0 \\ G_w \\ 0 \end{bmatrix} e_0 \end{aligned} \quad (16)$$

where the subscripts of the variables are used to specify specific the connecting bilayers between aqueous volumes labeled in Figure 26, G_w is the conductance to the source, and e_0 is a triangular input to mimic the recorded data from previous results. The capacitance matrix C in this case is non-singular, allowing for its inversion and the separation of the ODEs. The protein conductance is modeled as:

$$\begin{aligned} P_{12} &= \begin{cases} m_1, & \text{if } V_1 \geq V_2 \\ m_2, & \text{if } V_1 < V_2 \end{cases} \\ P_{13} &= \begin{cases} m_3, & \text{if } V_1 \geq 0 \\ m_4, & \text{if } V_1 < 0 \end{cases} \\ P_{24} &= \begin{cases} m_5, & \text{if } V_2 \geq V_4 \\ m_6, & \text{if } V_2 < V_4 \end{cases} \\ P_{34} &= \begin{cases} m_7, & \text{if } V_4 \leq 0 \\ m_8, & \text{if } V_4 > 0 \end{cases} \end{aligned} \quad (17)$$

For numerical simplicity, the exponential decay properties of Equation (14) are excluded from this simulation because the system is simulated at a low frequency (1 mHz) and the time constants of the closing barrel would have little effect on the simulated value. This low applied frequency also ensures that the two node solution method remains appropriate for the simulation.

This conductance model for the protein α HL and the engineered derivative 7R- α HL provides approximations for the average conductance of multiple pores within a bilayer. Each individual pore has a certain conductance level and dynamics that are not captured with the model that may be a function of the concentration or other variables. Therefore, the conductance model is adjusted for individual trials to obtain a closer match to measured data and the specific changes are mentioned when a comparison is presented. The values for the protein conductance levels is equivalent to 7 channels per membrane for a total open conductance of 6.3 nS.

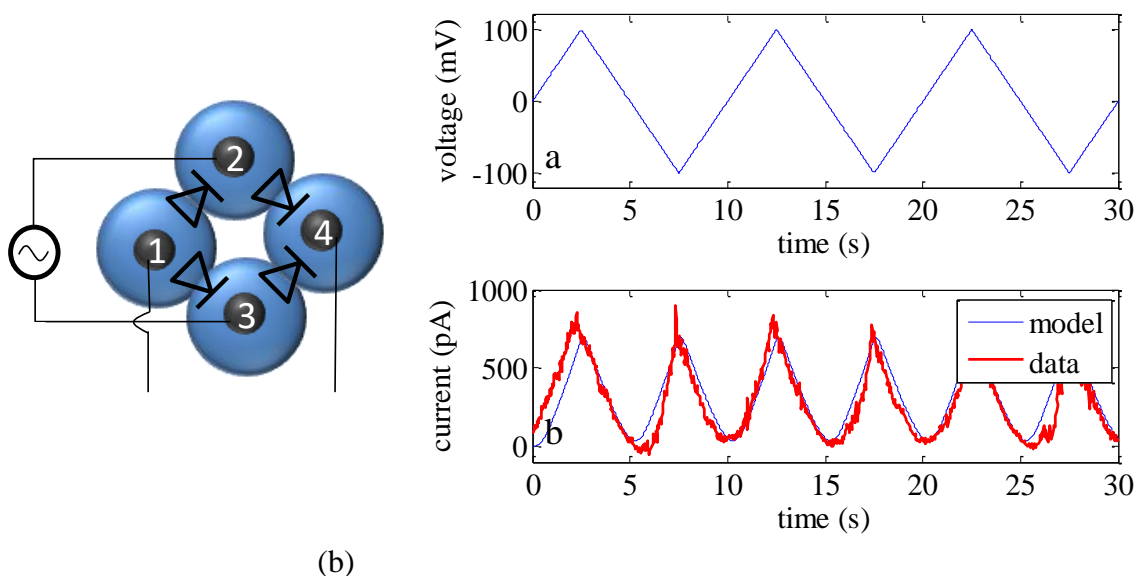


Figure 26 - a) A four droplet, four-unit cell system with the 7R- α HL proteins oriented as shown by the diodes schematics and b) the traced data compared to the simulated ion currents.

The membrane potentials are solved using Equation (16) and Equation (17) with a simulated input to the system consisting of a 100 mV triangular wave at 10 mHz (allowing for the two node simplification). The ion currents through each bilayer are calculated using Ohm's law and the ion current across droplets 4 and 1 are the sum of the currents into and out of those volumes through KCL. Figure 26b shows the system input, the measured ion current data from prior work, and the simulated ion current.

The results from the coupled model closely match the experimental results and retain the desired full-wave rectification behavior. If the rectifying pores were not included in the simulation, the potential in droplets 1 and 4 would remain equal, resulting in no measured current across the connecting wire. This bilayer network example shows how the model may be used to estimate the membrane potentials at different points of a bilayer network when a potential is applied at some point within the network. The membrane potential is used in conjunction with the stimuli-responsive biomolecule conductance models to estimate the ion currents through a bilayer. The conductance and network modeling allows an engineer to vary the parameters of the system and see how those variations alter the system performance.

In natural cellular systems the dimensions of the cells are often reduced in comparison to the droplet interface bilayers constructed here. This allows for these measured shifts in voltage to be accompanied by meaningful changes in the concentration of ions inside the droplets. These ionic

concentrations are used in natural systems for determining the states of the cell through osmotic pressures, activation of chemically-dependent biomolecules, and other phenomena. Referring back to the characteristic droplet dimension r , the ratio of the droplet volume to the bilayer surface area scales directly with r . Since this ratio is increased for the artificial biomolecular networks these volume-dependent ionic shifts require more time, and the change in concentration accompanied by the area-dependent changes in membrane potential are generally negligible. Future work will focus on combining these ionic gradients for a more accurate comparison to natural cellular systems as the droplet dimensions are reduced to better approximations of natural networks.

4. Characterization of biomolecular materials under a range of standardized conditions that enable direct comparison to the effectiveness of more traditional types of multifunctional materials.

A specialized test setup was developed to enable controllable actuation of the bilayer as well as accurate mechanical and electrical measurements of the interface. The test setup consisted of one droplet anchored to the tip of a mobile capillary mounted on a piezoelectric actuator and a second droplet anchored to a fixed substrate. The tension in the artificial lipid bilayer membrane is modulated by horizontally oscillating the droplet anchored to the piezoelectric actuator (Figure 27), thereby distorting the shapes of the droplets (i.e. increasing the surface area of each droplet) and changing the contact angle between the water-oil interfaces. In this work, branched diphytanoyl phosphatidylcholine (DPhPC) is used to form bilayers. DPhPC bilayers neither oxidize nor exhibit phase transitions with temperature and thus are stable; they also have the advantage of high interfacial tension³². It is well established that the electrical properties of a lipid bilayer are modelled accurately by a high membrane resistance (typically in the giga-ohm range) in parallel with the membrane capacitance²⁷. Therefore, low-frequency sinusoidal oscillations applied to the DIB result in a harmonic variation in bilayer capacitance that correlates with a change in the bilayer area (Figure 28a). The electrical response of the DIB, free of MscL channels, was recorded simultaneously with video imaging of the droplets, while mechanically oscillated at frequencies ranging from 0.1 Hz up to 75 Hz, and peak-to-peak amplitudes ranging between 125 μm and 175 μm . These observations serve to form a basic understanding of the components of the mechano-electrical response of the DIB without MscL, and serve to provide a ‘baseline’ control for the subsequent recordings with MscL channels reconstituted within the membrane. No measurable conductive component or gating-like spikes are observed in the control (Figure 28a). This insures that the sub-conductive state events observed (when V23T-MscL is incorporated) are not simply random artefacts resulting from the bilayer oscillations and electrical recordings. The electrical responses of DIBs with V23T-MscL incorporated are also recorded in a broad range of transmembrane potentials (0–150mV) with no mechanical stimulus applied (Figure 28b). As previously observed, no gating-like spikes were

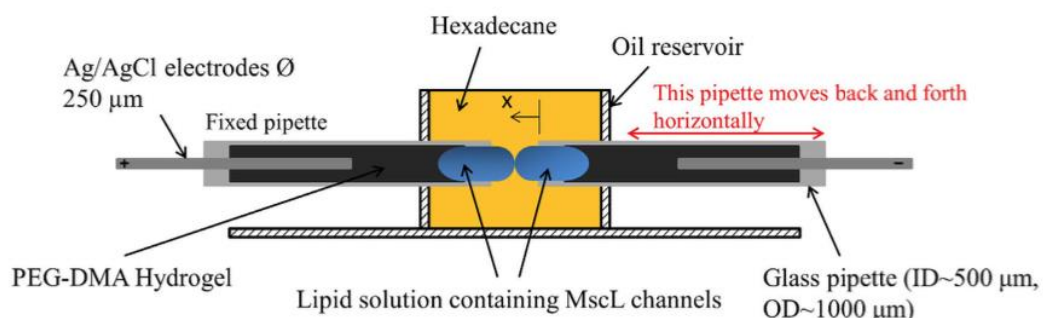


Figure 27: The experimental setup used to form the droplet interface bilayers, mechanically stimulate the droplets, and study MscL activity. The DIB supporting part consists of two hydrogel filled glass capillaries with inserted Ag/AgCl electrodes. Two lipid containing droplets are anchored to the tips of the micropipettes (ID $\sim 500\mu\text{m}$, OD $\sim 1000\mu\text{m}$), and placed within a cylindrical oil filled reservoir. The micropipette on the left is fixed and attached to the headstage of the Axopatch 200B amplifier, while the micropipette on the right is connected to a piezoelectric actuator which allows it to move horizontally.

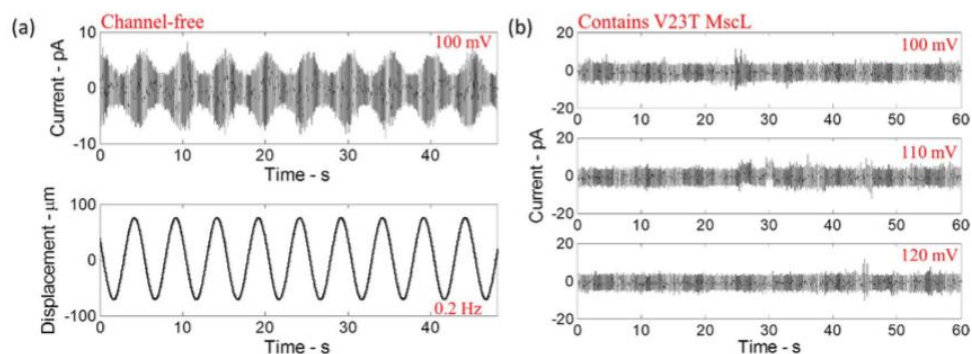


Figure 28: (a) The current response of the lipid bilayer (free of MscL channels) as droplets are oscillated at 0.2 Hz and 150 μm peak-to-peak amplitude. The current response is sinusoidal which corresponds to the change in the bilayer capacitance correlated with a change in the lipid bilayer area resulting from the sinusoidal oscillations of the droplets. (b) The current response of the lipid bilayer containing V23T-MscL channels when high transmembrane potentials are applied without mechanically stimulating the droplets.

recorded, indicating that creating tension in the membrane is essential for the gating of V23T-MscL. Note that all low amplitude ($\sim 5\text{pA}$) channel gating-like events, especially the ones in the 110mV trace, likely represent transient conductive defects in the dynamic membrane structure stabilized by the electric field. With the droplets of approximately 0.5mm in diameter, the initial bilayer area was approximately 0.0024 mm^2 . The generated currents in channel-free controls were small, reflecting a highly resistive lipid bilayer ($\sim 10\text{G}\Omega$).

In order to observe V23T-MscL-6His gating pattern in the native setting, we expressed the channel in MJF 465 *E. coli* cells⁴ and recorded traces from giant spheroplasts using standard patch-clamp technique. The gating response of the mutant in spheroplasts to mechanical stimuli (shallow negative pressure ramps ranging between 50 to 170mm Hg) under an applied potential of $\pm 40\text{mV}$, are shown in Fig. 3a. In a parallel effort, we have purified 6-His tagged V23T-MscL and reconstituted it in DPhPC liposomes. Recordings from liposome ‘blisters’ were performed, with mechanical stimuli applied in a similar fashion as previously mentioned, in order to observe single-channel events (Figure 29b). To compare conductance levels, both types of recordings were performed in the buffer of the same specific conductivity as used for DIBs. We found that the activities in both cases were essentially identical in terms of unitary conductance (3.5–3.8nS full openings designated by arrows in Fig. 3), with similar kinetic patterns. When activated at relatively low open probability, V23T-MscL exhibits a variety of short-lived sub-conductive states. According to the previous data^{6,33}, this mutant has a tension midpoint of 9.5mN/m (compared to 12–14mN/m for WT-MscL³³), yet the first opening events are reproducibly observed near 6mN/m. Based on this data, we anticipated that in DIBs V23T-MscL should start flickering at tensions between 6 and 7mN/m.

Transient MscL responses to harmonic compression

The incorporation of V23T-MscL into DIBs is achieved by introducing proteoliposomes into both droplets. A low-threshold V23T mutant of MscL generates reliable activities including sub-conductive states as well as full opening events (Figure 30a) when mechanically stimulated and a DC potential is applied to the membrane. These events are identical to those recorded using the

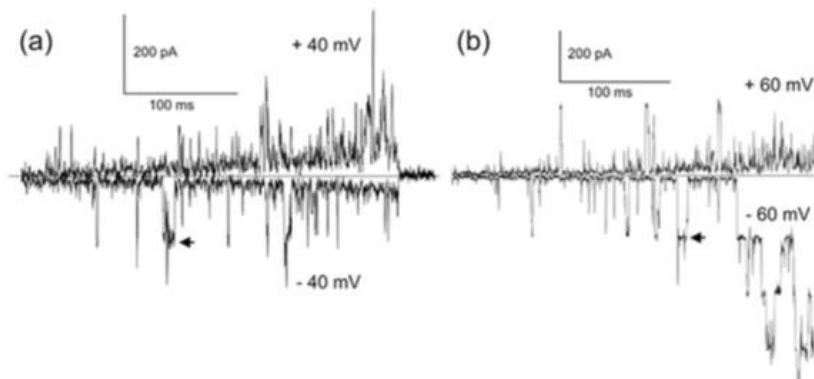


Figure 29: V23T-MscL activities recorded using standard patch-clamp technique in *E. coli* giant MJF465 spheroplasts (a) and in DPhPC liposomes reconstituted with purified protein (b). The mechanical stimuli in both cases are shallow ramps of negative pipette pressure (suction) to 50–170 mm Hg. Both traces recorded in a symmetric 400mM KCl, 20mM MgCl₂ and 10mM CaCl₂ buffer characterized with the same conductivity as the buffer used for DIB formation. Conductance levels of 3.5–3.8nS indicated by black arrows correspond to the fully open channels occurring amid various sub-conductive states.

patch-clamp technique from intact inner *E. coli* membranes and liposomes reconstituted with the purified V23T-MscL (Figure 29). The mechanical stimulus is applied through axial sinusoidal displacements of one droplet toward and away from another with a frequency of 0.2Hz and peak-to-peak amplitude of 150 μ m. It is observed that the gating of V23T-MscL mostly occurs at transmembrane potentials above 80mV and low oscillation frequencies (<1Hz). Gating occurs exclusively near the point of shortest separation where both the contact area and fractional change in droplet area are maximal, while the lipid bilayer contact angle between the droplets (monolayers) is minimal.

To illustrate this observation, the representative DIB current traces, each covering one stimulation cycle, are plotted in the polar form indicating the position of the V23T-MscL opening events relative to the phase of the mechanical displacement (Figure 30c). The results show that the channel consistently activates between 90 and 120 degrees. This region on the polar plot corresponds to the position near peak compression (where the sinusoidal mechanical input reaches maximum amplitude) and maximum bilayer area. The current is proportional to the capacitance of the bilayer $I(t) = V \frac{dC}{dt}$, which in turn obeys the same sine wave law

($C(t) \sim A \sin(\omega t)$) implying that there is a 90-degree phase shift between the actual change in bilayer area (i.e. capacitance) and the recorded capacitive current. This explains why the gating is seen in the 90–120 degree region on the current polar plot. Identical behaviour is observed when the potential is increased to 100mV while a 0.2Hz sinusoidal oscillation is maintained (Figure 30b). The only difference seen is that the measured conductance levels are higher, which may indicate a greater expansion of the channel, due to an increased transmembrane potential.

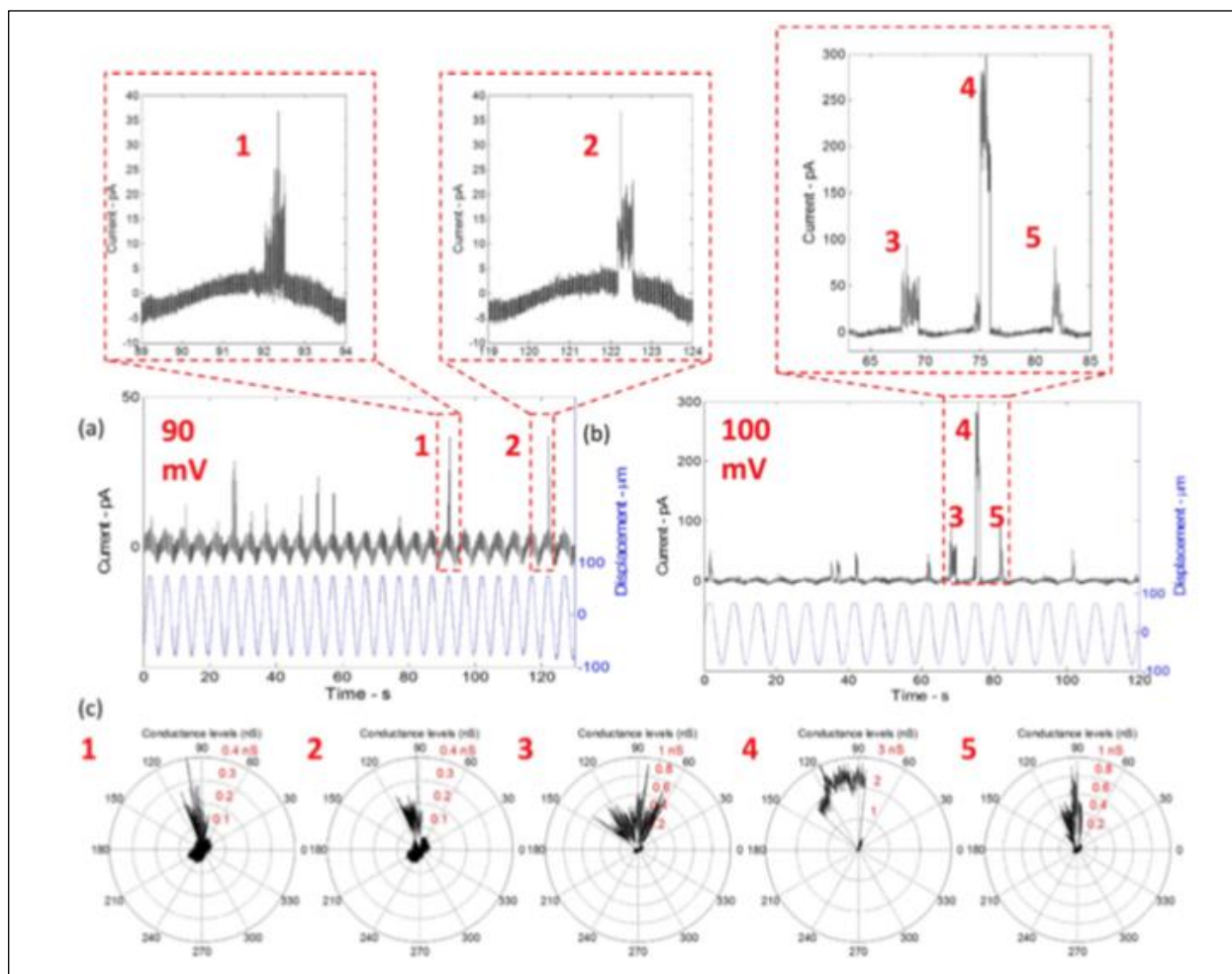


Figure 30: (a,b) The current response of the bilayer containing V23T-MscL mutant channels at 0.2 Hz (sinusoidal) and an applied transmembrane potential of 90 and 100mV respectively. The shape of the current response is sinusoidal which corresponds to a sinusoidal change in bilayer capacitance as a consequence of the bilayer area change. The currents spikes at the peak of each cycle (i.e. maximum bilayer area) correspond to sub-conductance gating events of the MS channels. (c) Each of the six cycles is plotted in polar form indicating that the gating events consistently occur between 90 and 120 degrees.

We have also analysed the amplitude distribution of opening events recorded over 110 cycles under ‘near-optimal’ stimulation with 0.2Hz/87.5 μm sinusoidal droplet oscillations and a transmembrane potential of 100mV (Figure 31). Most of the events represent low sub-conductive states, consistent with low-open probability patch-clamp traces presented in Figure 29 and previous analysis. Full-openings of 3.1nS amplitude constitute only 3% of all events.

Effects of the displacement amplitude and applied transmembrane potential

The gating of the V23T-MscL channels is observed to be dependent on the transmembrane electrical potential, as well as the amplitude of oscillations. These findings are highlighted in Figure 32 where the current responses of the DIB are recorded for three different oscillation amplitudes ($\pm 62.5\mu\text{m}$; $\pm 75\mu\text{m}$; $\pm 87.5\mu\text{m}$), while a frequency of 0.2Hz is maintained. At each oscillation amplitude, the transmembrane potential is varied between 20mV and 100mV. Figure 6 shows the polar plots of different cycles for the three different amplitudes each at a specific transmembrane electrical potential. In the $\pm 62.5\mu\text{m}$ displacement case, no gating occurs, where

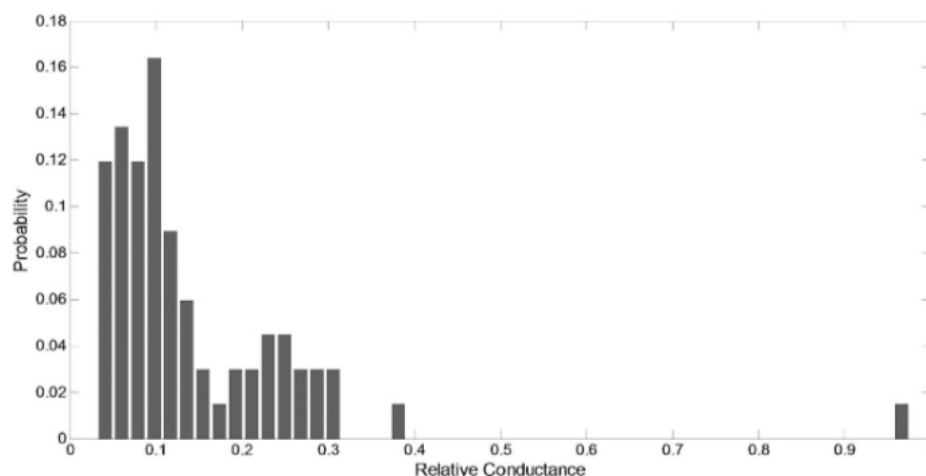


Figure 31: The amplitude histogram of V23T-MscL opening events obtained from multiple traces including 110 oscillation cycles. The droplets are subjected to periodic oscillation (0.2Hz and 87.5 μ m amplitude) and a transmembrane potential of 100mV for several minutes and a total of 52 events were analysed. Under these conditions the probability of seeing an opening event per cycle was 0.47. The histogram shows that low-conductance sub-states are more likely to occur under the given testing conditions.

the results resemble those of the channel-free case. This means that the induced bilayer tension is not strong enough to make the channels open. As the amplitude of oscillations is increased to $\pm 75\mu$ m, MscL gating events are observed at transmembrane potentials higher than 80mV. Similar results are obtained for the $\pm 87.5\mu$ m, however, it is noticed that the conductance levels are higher compared to the lower amplitude case. The results imply that widening of the conductive pore can be achieved through an increase in bilayer tension produced by increased oscillation amplitude. The results presented in this section confirm that both the transmembrane applied potential and the degree of drop-let deformation are contributing in increasing the tension in the lipid bilayer membrane.

changes of the contact angle may generate tension sufficient for MscL gating. We therefore analysed the geometry of the DIB system using image processing techniques for images taken at different positions during the compression cycle. We found that the bilayer contact angle, θ_b , decreases while the bilayer contact area increases. At the bilayer interface, to maintain mechanical equilibrium the downward tension (i.e. the bilayer tension γ_b) should be equilibrated by an upward tension equivalent to the projections of both monolayers tensions (γ_m) on the plane of the bilayer interface. This relationship is illustrated through the Young-Dupré equation:

$$\gamma_b = 2\gamma_m \cos\left(\frac{\theta_b}{2}\right)$$

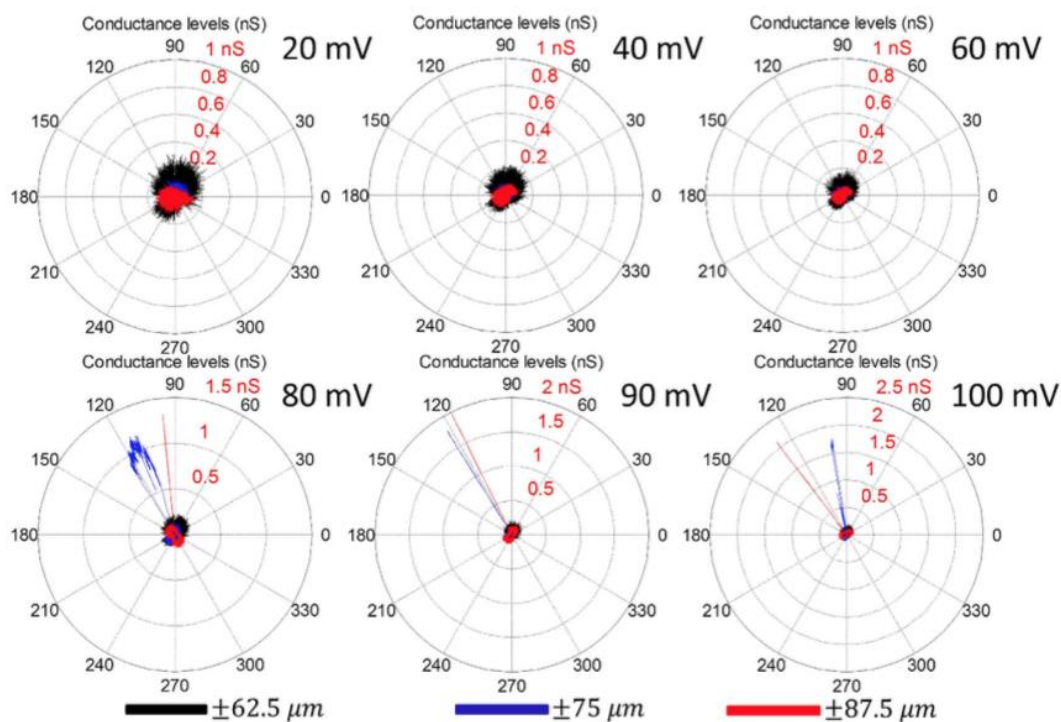


Figure 32: Gating dependence on the amplitude of droplet displacement and voltage. The droplets are oscillated at three different amplitudes. At each amplitude the applied electric potential is varied between 20mV and 100mV. The results in black, corresponding to the lowest amplitude ($\pm 65\mu\text{m}$), and show that no MS channel activity occur at all potentials. However, as the amplitude is increased to $\pm 75\mu\text{m}$, gating events occur at potentials starting from 80mV up to 100mV. The results at the highest amplitude ($\pm 87.5\mu\text{m}$) are similar to the previous case however the conductance levels are higher which may be a result of opening the MS channels further as the tension in the bilayer is higher at higher oscillation amplitudes.

The equation above suggests that γ_b is always lower than $2\gamma_m$, and for this to be true, the Plateau-Gibbs border must move away from the centre of the bilayer in order to increase γ_b . Note that at the Plateau-Gibbs border, the monolayers (water-oil interface) are near spherical according to the Young-Laplace equation²². Therefore, under conditions of constant volume, the area of the monolayer covering the entire water-oil interface in both compressed droplets increases. The relative expansion of the droplets is measured at different frequencies while maintaining a 100 mV transmembrane potential. Our results (Figure 33c) show that at 0.2 Hz the droplet relative area change is approximately 2.5%. However, as we increased the frequency of oscillation to 7.5 Hz this value dropped to approximately 0.1%. The elastic modulus for isothermal area compression or extension is defined in terms of the mechanical properties of the monolayer as follows:

$$\Delta\gamma_m = K_m \left(\frac{\Delta A_m}{A_m} \right)_T$$

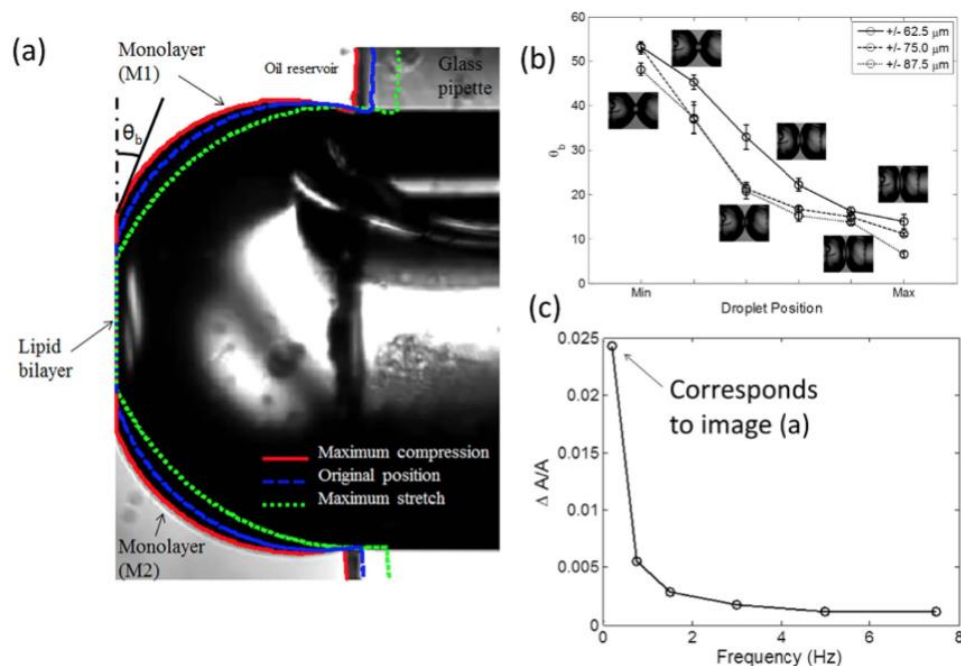


Figure 33: Changes in droplet areas and contact angles revealed by imaging and area calculations in the course of cyclic mechanical stimulation. (a) The zoomed-in view of the one droplet and determination of the entire interfacial area, the bilayer area, and the contact angle. (b) The bilayer angle as a function of the displacement. (c) The relative area changes as a function of frequency of oscillation.

The tension increase in each monolayer can be written as the product of the elastic modulus (K_m) and the relative areal expansion of the interface. The compression/expansion elasticity modulus K_m for DPhPC monolayers has been recently estimated as about 120mN/m. Our results show that with a relative expansion ranging between 2% to 3%, the tension in each monolayer can reach 2.4–3.6mN/m. These monolayer tension values add up and result in 4–7 mN/m in the bilayer membrane which is sufficient to open V23T-MscL. Figure 33b shows the variation in bilayer angle value as the droplets are deformed. In this plot, “Min” refers to the minimum compression point where the droplets are furthest apart, while “Max” refers to the maximum compression point. θ_b is measured at different locations between the two extreme droplet positions. The results exhibit a decrease in θ_b during compression, which eventually results in an increase in the bilayer tension γ_b . Another important observation is that the angle at the maximum compression point is decreased as the oscillation amplitude is increased (i.e. the droplets are more compressed). At the point of maximum compression, θ_b is small (5–10 degrees), and as a result, γ_b is almost equal to $2\gamma_m$. The bilayer angle being too large, at the point of maximum separation (minimum compression), explains the reason why gating is not seen at the point of maximum separation where the area of the monolayer still increased.

Discussion

MscL is a well-characterized tension-activated molecular valve. With genetic and chemical modifications of its gates, we can engineer this channel with predicted thresholds for activation by tension. We chose V23T, a mild gain-of-function mutant, which is firmly closed at rest but opens at lower tension than the one needed to gate WT-MscL. We deliberately avoided severe

gain-of-function mutants such as V23D or G22E, which tend to gate spontaneously. We consistently saw V23T-MscL channel activities in response to simultaneous mechanical and electrical stimulation in DIBs. There is a real perspective that such a channel could be used as a transducer in biomolecular stimuli-responsive materials, especially that we found that the protein in reconstituted DPhPC liposomes remained functional for at least three months, and thus it remains stable in liposomes and functional after being reconstituted within the lipid-stabilized oil-water interface.

To date, patch-clamp (which requires bulky equipment) has been the most convenient technique to study the activity of MscL, since it permits clamping of both voltage and tension. However, biomolecular engineering of sensory and conversion devices implies compactness. In DIBs, until present day, tension cannot be clamped and therefore mechanosensitive channels can be stimulated only in a dynamic regime. Despite this, DIBs are emerging flexible platforms that could be adapted to many types of stimuli with the ability to be miniaturized. Here, we present the first study in which the activities of single bacterial MscL channels are directly recorded in a miniature DIB system without the use of a patch pipette or chemical modifications. The developed experimental technique is novel and important since it mimics the natural asymmetry of lipid membranes while changing the membrane tension profile. We successfully reconstituted V23T-MscL channels in the bilayer formed at the interface of two lipid encased droplets and the ability of the DIB to sense mechanical stimuli using bacterial MscL as a mechano-electrical transducer has been demonstrated. The channels self-assembled within the lipid bilayer membrane are activated when tension in the interfacial bilayer is generated. This is achieved by virtue of dynamic droplets' compression and relaxation through axial sinusoidal displacement of one droplet towards and away from the other. The resulting amplitudes of MscL conductance levels were similar to those recorded by patch-clamp indicating a fully-functional state of MscL in DIBs.

The factors leading to the activation of MscL in the DIB can be categorized as mechanical and electrical. A sufficiently high amplitude oscillation (~20% of the droplet diameter) is required to transmit tension to the bilayer. With a 2.5% maximal observed relative areal expansion of droplets and a monolayer elasticity modulus of 120mN/m we generated an increase in tension of about 3mN/m in each leaflet. With small bilayer angles, at peak compression, the increase in monolayer tension roughly doubled in the interfacial bilayer membrane. The estimated peak tension of about 6mN/m is near the threshold of the V23T-MscL activation curve, which evokes mainly sub-states and occasionally fully open-states. Our analysis shows that under the same conditions (i.e. 0.2 Hz frequency, 87.5 μ m amplitude, and transmembrane potential of 100mV) the gating probability per cycle of V23T channels is found to be around 47% (Figure 33). The distribution of conductance levels across several traces (Figure 31) shows that the majority of events are sub-conductive states and only in rare occasions (~3%) full openings are achieved. We also found that in the relaxation phase, when the droplets are furthest apart, the area of the droplet interface increased substantially leading to an increase in monolayer tension; however, the rise in interfacial bilayer tension is not significant due to large contact angle (~53°). Remarkably, the range of frequencies, in which we were able to see V23T-MscL activities, is narrow. At a frequency of 0.2Hz, which we found optimal for the chosen geometry, we observed that at peak compression the area of the contact bilayer increased and then decreased by 80% at the point of maximum separation. This “unzipping” of the contributing monolayers allowed the

droplets to regain a nearly spherical shape before the next compression phase. The droplets gradually returned to a spherical shape and regained their minimal area (at a given volume), thus enabling higher area and tension increase during the next compression cycle. At higher frequencies, as shown in Figure 33c, we observe a significantly smaller area expansion due to a delay in the monolayer “unzipping”. Therefore, the viscous resistance of the inter-monolayer gap to flow of the organic solvent (hexadecane) appears to be the natural “low-pass” mechanical filter in the DIB system. However, the presence of the lipid reservoir in the form of liposomes in each aqueous compartment makes the channel only respond to dynamic stimuli, imposing a “high-pass” filter. Transient channel activation, observed under harmonic stimulation, was the way to overcome the membrane tension relief, resulting from the incorporation of the lipid from the aqueous phase into the monolayers. In the course of harmonic deformation of the droplets at 0.2Hz, the compression phase lasts for 1.25s, during which sufficient expansion of the interfaces and activation tension (~ 6 mN/m) is achieved. The question is, how quickly and how far the tension may relax due to new lipid incorporation? According to the most recent data, the characteristic time of DPhPC liposome equilibration with the monolayer at the water-oil interface is 180–200s, eventually reaching an equilibrium tension of ~ 1 mN/m. The tension in the compound bilayer at equilibrium is thus estimated to be ~ 2 mN/m, which is far below the activation threshold for V23T-MscL. However, this relaxation process is slow. Additionally, relatively low lateral diffusion rate of the DPhPC lipid ($\sim 18.1 \times 10^{-8}$ cm²/s)³⁶, will be another factor that slows tension equilibration across each interfacial monolayer. For this reason, tension in the interfacial bilayer will be minimally affected by the incorporation of liposomes from aqueous reservoirs under the chosen 0.2Hz regime of harmonic stimulation.

Speaking about transmembrane voltage, we found that a 100 mV transmembrane potential is required for the activation of V23T-MscL. Also, the membrane tension may be modulated by the transmembrane voltage. We believe that the combination of different physical parameters, resulting from the mechanical deformation of the droplets and transmembrane voltage, is leading to the gating of MscL in the DIB. It is also important to note that we are dealing with a stochastic and not deterministic behaviour near the threshold, and since we are at the foot of activation curve, we do not expect activation with every cycle.

Further investigation will include understanding the physics of mechanoelectrical transduction in the DIB in order to increase the sensitivity of MscL to a mechanical stimulus. Ways to increase the bandwidth of the system may include miniaturization, reducing the lipid concentration in the bulk to slow down the lipid exchange, chemical cross-linking of lipids, and preparation of DIBs with hydrogels. These findings are fascinating because on one hand, with the use of MscL as a “strain gauge”, we will have the opportunity to understand how tension is created at the interface of a DIB. Additionally, this system will help us learn more about MscL and the ways external forces can be conveyed to its gate.

List of Peer-Reviewed Publications

1. Bhadauria R, Aluru NR. Multiscale modeling of electroosmotic flow: Effects of discretization, enhanced viscosity, and surface friction. *Journal of Chemical Physics*. 2017;146(18):1.
2. Bhadauria R, Aluru NR. A multiscale transport model for Lennard-Jones binary mixtures based on interfacial friction. *Journal of Chemical Physics*. 2016;145(7):1.
3. Bhadauria R, Sanghi T, Aluru NR. Interfacial friction based quasi-continuum hydrodynamical model for nanofluidic transport of water. *Journal of Chemical Physics*. 2015;143(17):1.
4. Boreyko JB, Mruetusatorn P, Sarles SA, Retterer ST, Collier CP. Evaporation-induced buckling and fission of microscale droplet interface bilayers. *Journal Of The American Chemical Society*. 2013;135(15):5545-5548. doi:10.1021/ja4019435.
5. Boreyko JB, Polizos G, Datskos PG, Sarles SA, Collier CP. Air-stable droplet interface bilayers on oil-infused surfaces. *Proceedings of the National Academy of Sciences of the United States of America*. 2014;111(21):7588-7593. doi:10.1073/pnas.1400381111.
6. Elio J. Challita, Joseph S. Najem, Rachel Monroe, Donald J. Leo, Eric C. Freeman. Encapsulating Networks of Droplet Interface Bilayers in a Thermoreversible Organogel. *Scientific Reports*. 2018;(1):1. doi:10.1038/s41598-018-24720-5.
7. Creasy MA, Freeman EC, Philen MK, Leo DJ. Deterministic model of biomolecular networks with stimuli-responsive properties. *Journal of Intelligent Material Systems & Structures*. 2015;26(8):921
8. Farimani AB, Aluru NR, Tajkhorshid E. Thermodynamic insight into spontaneous hydration and rapid water permeation in aquaporins. *Applied Physics Letters*. 2014;105(8):1.
9. Farimani AB, Wu Y, Aluru NR. Rotational motion of a single water molecule in a buckyball. *Physical Chemistry Chemical Physics (PCCP)*. 2013;15(41):17993
10. FARIMANI, A. B.; HEIRANIAN, M.; ALURU, N. R. Nano-electro-mechanical pump: Giant pumping of water in carbon nanotubes. *Scientific Reports*, [s. l.], p. 26211, 2016.
11. Freeman EC, Najem JS, Sukharev S, Philen MK, Leo DJ. The mechano-electrical response of droplet interface bilayer membranes. *SOFT MATTER*. 2016;(12):3021.
12. Heiranian M, Yanbin Wu, Aluru NR. Molybdenum disulfide and water interaction parameters. *Journal of Chemical Physics*. 2017;147(10):1

13. Heiranian M, Farimani AB, Aluru NR. Water desalination with a single-layer MoS₂ nanopore. *Scientific Reports*. October 2015:8616
14. HEIRANIAN, M.; FARIMANI, A. B.; ALURU, N. R. Water desalination with a single-layer MoS₂ nanopore. *Nature Communications*, [s. l.], v. 6, n. 10, p. 8616, 2015
15. Mashayak SY, Aluru NR. Langevin-Poisson-EQT: A dipolar solvent based quasi-continuum approach for electric double layers. *Journal of Chemical Physics*. 2017;146(4):1.
16. Mashayak SY, Jochum MN, Koschke K, Aluru NR, Rühle V, Junghans C. Relative Entropy and Optimization-Driven Coarse-Graining Methods in VOTCA. *PLoS ONE*. 2015;10(7):1-20
17. Mashayak SY, Jochum MN, Koschke K, Aluru NR, Rühle V, Junghans C. Relative Entropy and Optimization-Driven Coarse-Graining Methods in VOTCA. *PLoS ONE*. 2015;10(7):1.
18. Motevaselian MH, Aluru NR. An EQT-based cDFT approach for thermodynamic properties of confined fluid mixtures. *Journal of Chemical Physics*. 2017;146(15):1
19. Mruetusatorn P, Boreyko JB, Venkatesan GA, Sarles SA, Hayes DG, Collier CP. Dynamic morphologies of microscale droplet interface bilayers. *Soft matter*. 2014;10(15):2530-2538. doi:10.1039/c3sm53032a.
20. Mruetusatorn P, Polizos G, Datskos PG, et al. Control of membrane permeability in air-stable droplet interface bilayers. *Langmuir: The ACS Journal Of Surfaces And Colloids*. 2015;31(14):4224-4231. doi:10.1021/la504712g.
21. Najem JS, Dunlap MD, Rowe ID, et al. Activation of bacterial channel MscL in mechanically stimulated droplet interface bilayers. *SCIENTIFIC REPORTS*. 5. doi:10.1038/srep13726.
22. Najem JS, Dunlap MD, Yasmann A, et al. Multifunctional, Micropipette-based Method for Incorporation And Stimulation of Bacterial Mechanosensitive Ion Channels in Droplet Interface Bilayers. *JOVE-JOURNAL OF VISUALIZED EXPERIMENTS*. (105). doi:10.3791/53362.
23. Najem JS, Freeman EC, Yasmann A, Sukharev S, Leo DJ. Mechanics of Droplet Interface Bilayer “Unzipping” Defines the Bandwidth for the Mechanotransduction Response of Reconstituted MscL. *ADVANCED MATERIALS INTERFACES*. 4(3). doi:10.1002/admi.201600805.
24. Joseph S. Najem, Ian Rowe, Andriy Anishkin, Donald J. Leo, Sergei Sukharev. The voltage-dependence of MscL has dipolar and dielectric contributions and is governed by

- local intramembrane electric field. *Scientific Reports*. 2018;(1):1. doi:10.1038/s41598-018-31945-x.
25. Nandigana VVR, Jo K, Timperman A, Aluru NR. Asymmetric-Fluidic-Reservoirs Induced High Rectification Nanofluidic Diode. *Scientific Reports*. 2018;8(1):1
 26. Niroomand H, Venkatesan GA, Sarles SA, Mukherjee D, Khomami B. Lipid-Detergent Phase Transitions During Detergent-Mediated Liposome Solubilization. *The Journal of membrane biology*. 2016;249(4):523-538. doi:10.1007/s00232-016-9894-1.
 27. Nguyen M-A, Srijanto B, Collier CP, Retterer ST, Sarles SA. Hydrodynamic trapping for rapid assembly and in situ electrical characterization of droplet interface bilayer arrays. *Lab On A Chip*. 2016;16(18):3576-3588. doi:10.1039/c6lc00810k.
 28. Pour MM, Lashkov A, Radocea A, et al. Laterally extended atomically precise graphene nanoribbons with improved electrical conductivity for efficient gas sensing. *Nature Communications*. 2017;8(1):1
 29. Sanghi T, Bhadauria R, Aluru NR. Memory effects in nanoparticle dynamics and transport. *Journal of Chemical Physics*. 2016;145(13):1
 30. Sanghi T, Aluru NR. A combined quasi-continuum/Langevin equation approach to study the self-diffusion dynamics of confined fluids. *Journal of Chemical Physics*. 2013;138(12):124109.
 31. Sanghi T, Aluru NR. Thermal noise in confined fluids. *Journal of Chemical Physics*. 2014;141(17):1
 32. Tamaddoni N, Sarles SA. Toward cell-inspired materials that feel: measurements and modeling of mechanotransduction in droplet-based, multi-membrane arrays. *Bioinspiration & biomimetics*. 2016;11(3):036008. doi:10.1088/1748-3190/11/3/036008.
 33. Tamaddoni N, Taylor G, Hepburn T, Michael Kilbey S, Sarles SA. Reversible, voltage-activated formation of biomimetic membranes between triblock copolymer-coated aqueous droplets in good solvents. *Soft Matter*. 2016;12(23):5096-5109. doi:10.1039/c6sm00400h.
 34. Taylor GJ, Heberle FA, Seinfeld JS, Katsaras J, Collier CP, Sarles SA. Capacitive Detection of Low-Enthalpy, Higher-Order Phase Transitions in Synthetic and Natural Composition Lipid Membranes. *Langmuir: The ACS Journal Of Surfaces And Colloids*. 2017;33(38):10016-10026. doi:10.1021/acs.langmuir.7b02022.
 35. Taylor GJ, Sarles SA. Heating-enabled formation of droplet interface bilayers using *Escherichia coli* total lipid extract. *Langmuir: The ACS Journal Of Surfaces And Colloids*. 2015;31(1):325-337. doi:10.1021/la503471m.

36. Taylor GJ, Venkatesan GA, Collier CP, Sarles SA. Direct in situ measurement of specific capacitance, monolayer tension, and bilayer tension in a droplet interface bilayer. *Soft Matter*. 2015;11(38):7592-7605. doi:10.1039/c5sm01005e.
37. Venkatesan GA, Sarles SA. Droplet immobilization within a polymeric organogel improves lipid bilayer durability and portability. *Lab On A Chip*. 2016;16(11):2116-2125. doi:10.1039/c6lc00391e.
38. Venkatesan GA, Taylor GJ, Basham CM, Brady NG, Collier CP, Sarles SA. Evaporation-induced monolayer compression improves droplet interface bilayer formation using unsaturated lipids. *Biomicrofluidics*. 2018;12(2):024101. doi:10.1063/1.5016523.
39. Venkatesan GA, Lee J, Farimani AB, et al. Adsorption Kinetics Dictate Monolayer Self-Assembly for Both Lipid-In and Lipid-Out Approaches to Droplet Interface Bilayer Formation. *Langmuir : the ACS journal of surfaces and colloids*. 2015;31(47):12883-12893. doi:10.1021/acs.langmuir.5b02293.
40. Yanbin Wu, Wagner LK, Aluru NR. Hexagonal boron nitride and water interaction parameters. *Journal of Chemical Physics*. 2016;144(16):1
41. Yanbin Wu, Wagner LK, Aluru NR. The interaction between hexagonal boron nitride and water from first principles. *Journal of Chemical Physics*. 2015;142(23):1